Predictable Patterns of the Atmospheric Low-Level Circulation over the Indo-Pacific Region in Project Minerva: Seasonal Dependence and Intraensemble Variability

TUANTUAN ZHANG

School of Atmospheric Sciences, Sun Yat-Sen University, Guangzhou, China

BOHUA HUANG

Department of Atmospheric, Oceanic, and Earth Sciences, and Center for Ocean–Land–Atmosphere Studies, George Mason University, Fairfax, Virginia

SONG YANG

School of Atmospheric Sciences, and Guangdong Province Key Laboratory for Climate Change and Natural Disaster Studies, and Institute of Earth Climate and Environment System, Sun Yat-Sen University, Guangzhou, China

JAMES L. KINTER III

Department of Atmospheric, Oceanic, and Earth Sciences, and Center for Ocean–Land–Atmosphere Studies, George Mason University, Fairfax, Virginia

ABSTRACT

The predictable patterns and intraensemble variability of monthly 850-hPa zonal wind over the tropical Indo-Pacific region are investigated using 7-month hindcasts for 1983–2009 from Project Minerva. When applied to the ensemble hindcasts initialized on 1 May and 1 November, a maximum signal-to-noise empirical orthogonal function analysis identifies the patterns of high predictability as the hindcasts progress. For both initial months, the most predictable patterns are associated with El Niño–Southern Oscillation (ENSO). The second predictable patterns with May initialization reflect the anomalous evolution of the western North Pacific (WNP) monsoon, characterized by a northward shift of the WNP anomalous anticyclone/cyclone in summer and a southward shift in fall. The intraensemble variability shows a strong seasonality that affects different predictable patterns in different seasons. For May initialization, the dominant patterns of the ensemble spread bear some resemblance to the predictable WNP patterns in summer and ENSO patterns in fall, which reflect the noise-induced differences in the evolution of the predictable signals among ensemble members. On the other hand, the noise patterns with November initialization are dominated by the northern extratropical atmospheric perturbations from winter to early spring, which expand southward through the coupled footprinting mechanism to perturb the ENSO evolution in different ensemble members. In comparison, the extratropical perturbations in the Southern Hemisphere, most significant in early months with May-initialized predictions, are less effective in affecting the tropical circulation.

1. Introduction

The tropical Indo-Pacific region is characterized by complex geography, active atmosphere–ocean interaction, and major climate variation (Ramage 1968; Rasmusson and Carpenter 1983; Lau and Nath 1996; Torrence and Webster 1998; C.-P. Chang et al. 2000; Lau et al. 2000; Wang et al. 2000; Wang and Zhang 2002; Xie et al. 2002). Over this region, El Niño–Southern Oscillation (ENSO) is the dominant mode of interannual variability with large global influences, leading to significant environmental and socioeconomic consequences (Trenberth et al. 1998; McPhaden et al. 2006). Generally, ENSO events follow a similar life cycle, which develops during the boreal summer and fall, peaks in the boreal winter, and decays in the following spring (Philander et al. 1983; Hirst 1986; Jin

---

et al. 1994; Tziperman et al. 1994). The western North Pacific (WNP) anticyclonic (WNP-AC) anomaly, which is another major feature of the climate system in the region, begins to develop at the ENSO mature phase and persists to the following summer (Wang et al. 2000, 2003; Wang and Zhang 2002). This WNP-AC displays a northward shift from winter to the following summer (Xie et al. 2009). Three mechanisms have been proposed for the development and maintenance of the WNP-AC: a convectively coupled atmospheric Rossby wave response to suppressed convective heating (Wang et al. 2000); the "combination mode" of ENSO and the annual cycle (Stuecker et al. 2013, 2015); and the heat capacitor effect of the delayed tropical Indian Ocean (IO) warming, which forces atmospheric Kelvin waves into the WNP and induces northeasterly surface wind anomalies, resulting in regional divergence that generates the WNP-AC (Xie et al. 2009). An interbasin feedback with the northern IO may also prolong the WNP anomalies into the post–El Niño summer (Xie et al. 2016). Through this anomalous anticyclonic surface circulation or the Pacific–Japan (PJ) pattern (anomalous convective activity over the tropical northwestern Pacific and a meridional dipole of anomalous circulation in the lower troposphere; refer to Nitta 1987), ENSO further affects the climate over East Asia, including the East Asian summer monsoon (Wang et al. 2000; Kosaka et al. 2013). Besides the WNP-AC, the Indian Ocean dipole (IOD) and the Indian Ocean basinwide warming, which are the leading modes of climate variation in the tropical IO, are also closely associated with ENSO (e.g., Rasmusson and Carpenter 1982; Saji et al. 1999; Webster et al. 1999). Obviously, the large-scale atmospheric circulation plays a major role in variation and interaction of the climate systems over the tropical Indo-Pacific region; it can also transfer these impacts to the extratropical region (Wang et al. 2000; Cai et al. 2011; Jia et al. 2014; Sun and Zhou 2014).

Many studies have investigated the prediction and predictability of climate variations within the tropical Indo-Pacific region because of their widespread impacts on the global scale (Lin et al. 2008; Jiang et al. 2013; Zhu et al. 2015a,b; Zhang et al. 2016a,b). As a major source of predictability, ENSO is generally well predicted in dynamic models, but there is pronounced seasonal variation in prediction skill (e.g., Zebiak and Cane 1987; Battisti 1988; Balmaseda et al. 1995; Webster and Yang 1992; Luo et al. 2008). Common to most of the models, the prediction skill of ENSO decreases rapidly during the boreal spring (the so-called spring predictability barrier), and then sometimes rebounds in the following fall and winter (e.g., Zebiak and Cane 1987; Blumenthal 1991; Webster and Yang 1992). During the summer of the ENSO decaying year, the last echoes of ENSO are

confined to the Indo-WNP region, and the coupled PJ–IO mode [an interaction between IO sea surface temperature (SST) and the PJ pattern] provides seasonal predictability to the region (Xie et al. 2009; Chowdary et al. 2011; Kosaka et al. 2013).

Major improvements in model skill have been made in predicting climate variations over the tropical Indo-Pacific region during the past decades. However, the quality of seasonal predictions in this region is still far from satisfactory. Seasonal prediction errors can be generated by model systematic error, initial state error, and noise-driven error (Karspeck et al. 2006; Jia et al. 2012). While the model and initial state errors can potentially be reduced through model improvement and better observations, the noise-driven error is inherent to the dynamic system and limits its intrinsic predictability. For an ensemble seasonal prediction, the intraensemble spread characterizes both initial state inaccuracy and noise-driven error, which measures the reliability of the ensemble forecast (van der Linden and Mitchell 2009; Kirtman et al. 2014; Ma et al. 2017a,b). Understanding the mechanisms that determine the growth of intra-ensemble spread can provide insights into how these error sources are generated and how they may affect the predictable signals. For instance, Kosaka et al. (2013) indicated that the PJ–IO pattern emerges as the leading mode in both multimodel ensemble mean (signal) and intraensemble variability (noise) for the summer Indo-WNP region. This implies that the growth of the noise-driven error follows the same dynamics that governs the predictable signals. In this case, noise can cause the evolution of its counterpart predictable signal to differ among ensemble members and limit the predictability. By analyzing the intraensemble variability of seasonal hindcasts, Ma et al. (2017a) also found a strong coupling of the northern IO SST and the WNP-AC. Furthermore, ENSO may be stochastically forced by either processes that are partially ENSO state dependent (Kug et al. 2008), such as the Madden–Julian oscillation (MJO), or, to a lesser extent, the westerly wind bursts (WWBs; Lopez and Kirtman 2014), or intrinsic atmospheric variability that is not ENSO related. An example of the latter is the midlatitude atmospheric perturbations in the boreal winter and spring, which may expand equatorward and trigger an ENSO-like pattern via a seasonal footprinting mechanism (SFM; Vimont et al. 2001). Larson and Kirtman (2015, 2017) showed that the ENSO-independent equatorial wind develops via the ENSO-like feedback mechanism. In particular, stochastic wind perturbation on the equator in March is an important contributor to the spring predictability barrier (Penland and Sardeshmukh 1995; Penland 1996). It is clear that both types of random perturbations contribute to the

uncertainty of ENSO prediction (e.g., Penland and Sardeshmukh 1995; Penland 1996; Vimont et al. 2001; Zhang and Gottschalck 2002; Vimont et al. 2003; Hendon et al. 2007). Overall, understanding prediction uncertainty and its associated mechanism is vital to the improvement of model prediction skill and to the determination of the ultimate limit of such predictability.

In a recent study, Zhang et al. (2018) examined the predictive skill and predictable patterns of the 850-hPa zonal wind over the Indo-Pacific region, using the National Centers for Environmental Prediction (NCEP) Climate Forecast System, version 2 (CFSv2), reforecast dataset. They found that the most predictable patterns are associated with ENSO developing and maturing phases, which are predictable at multiseason lead (Zhang et al. 2018). The second most predictable patterns are more seasonally dependent, including the ENSO decaying phase during winter and spring and the WNP monsoon and IOD in summer and fall, respectively (Zhang et al. 2018). Our study verifies and extends their results using the hindcast dataset from another major seasonal forecast system. We focus on tracking predictable physical processes that evolve with season and lead time as well as the intraensemble variability of atmospheric low-level circulation over the tropical Indo-Pacific domain, which has not been fully understood heretofore. We also analyze the evolution of the predictable patterns with lead time and season. Furthermore, we examine the spatial–temporal structure of the intraensemble variability and how the ensemble spread may influence the predictable signals. This paper is arranged as follows: In section 2, we describe the hindcast and observational data and the analysis method. In section 3, predictive skill of 850-hPa zonal wind over the tropical Indo-Pacific domain is evaluated. In section 4, we analyze the seasonal evolution of the predictable ENSO patterns and WNP monsoon patterns. Intraensemble variability of the atmospheric low-level circulation over the tropical Indo-Pacific region and its associated mechanism are presented in section 5. Finally, a summary of the study and further discussion are included in section 6.

2. Model, data, and methods

Project Minerva is a collaborative project between the Center for Ocean–Land–Atmosphere Studies (COLA) and the European Centre for Medium-Range Weather Forecasts (ECMWF). It is an extension of Project Athena, a collaboration of weather–climate modelers and high-end computing experts from five international institutions, including the ECMWF and COLA, to test whether representing mesoscale and subsynoptic

processes in atmospheric general circulation models (AGCMs) can improve climate simulations (Kinter et al. 2013). Applying this concept to seasonal forecasting, Project Minerva employs a state-of-the-art coupled operational long-range prediction system based on the ECMWF Seasonal Forecast System 4 (System 4; Molteni et al. 2011). The ocean component is the Nucleus for European Modelling of the Ocean (NEMO; Madec 2008), version 3.0. Its discretization is on the ORCA1 grid, with a horizontal resolution of about $1°$ (with equatorial refinement of $\frac{1}{3}°$) and 42 vertical levels. For the atmospheric component, the ECMWF Integrated Forecast System (IFS) cycle 38r1 was applied with three different horizontal resolutions at T319, T639, and T1279, which correspond approximately to 62-, 31-, and 16-km grid spacing, respectively. The ocean and atmosphere are coupled every 3 h. The configurations for Project Minerva depicted above are similar to the operational ECMWF System 4, except for higher atmospheric resolutions.

The initial states of the ensemble hindcasts are from the initial conditions used for the operational ECMWF IFS system (Molteni et al. 2011). Specifically, the unperturbed atmospheric initial conditions are from the ERA-Interim generated by the ECMWF atmospheric data assimilation system (Dee et al. 2011). The land surface initial conditions derived as the output of an offline run of the Hydrology Tiled ECMWF Scheme of Surface Exchanges over Land (HTESSEL) forcing by the ERA-Interim data (e.g., precipitation, solar radiation, near-surface temperature, winds, and humidity; Molteni et al. 2011). The ocean initial conditions are from the Ocean Reanalysis System 4 (ORA-S4; Balmaseda et al. 2013), which has five ensemble members generated by an ocean data assimilation system. To generate the ensemble members, the five members of the ORA-S4 analyses are further perturbed by applying SST perturbations with associated subsurface projections. The atmospheric initial conditions are also perturbed using the operational Ensemble Prediction System (EPS) to calculate singular vectors (Molteni et al. 2011). The first 15 perturbed members are used as initial states for this set of hindcast runs. More details about the prediction system, including its initialization and ensemble generation, can be found in Molteni et al. (2011). The Minerva experimental design was further described in Zhu et al. (2015b) and Manganello et al. (2016).

Our analysis focuses on the 7-month hindcasts initialized on 1 May and 1 November during 1983–2009, consisting of 15 members for the T639 configuration. A previous study by Zhu et al. (2015b) demonstrated that the effect of atmospheric model component resolution

on the tropical SST prediction skill is relatively small. Our preliminary analysis of the tropical low-level winds is largely consistent with their result. Therefore, we mainly use the T639 outputs to demonstrate our results in this paper, but we will comment on potential effects of model resolution on certain aspects in the final section of the paper. For convenience, hindcast ensembles of 0-month lead, 1-month lead, . . . , and 7-month lead are denoted as LM0, LM1, . . . , and LM7, respectively. For observational verification, the monthly analyses of SST from the National Oceanic and Atmospheric Administration optimally interpolated SST analysis (Reynolds et al. 2007), sea level pressure (SLP) and 850-hPa wind from the NCEP Climate Forecast System Reanalysis (Saha et al. 2010), and precipitation from the Climate Prediction Center (CPC) Merged Analysis of Precipitation (CMAP; Xie and Arkin 1997) are used in this study.

To identify the most predictable patterns of 850-hPa zonal wind over the Indo-Pacific region, the empirical orthogonal function (EOF) analysis with maximized signal-to-noise ratio (MSN) is applied. The MSN EOF is an effective statistical technique to extract the predictable signals from an ensemble of hindcasts and maximizes the signal-to-noise ratio in a moderate ensemble size (Allen and Smith 1997; Venzke et al. 1999; P. Chang et al. 2000; Sutton et al. 2000; Huang 2004). In general, for an ensemble simulation, its ensemble mean is composed of signals and the residual of internal noise, the latter of which approaches zero when the ensemble size approaches infinity. Correspondingly, the ensemble mean covariance matrix $\mathbf{C}_M$ can be decomposed into a signal $\mathbf{C}_S$ and a residual noise $\mathbf{C}_R$ covariance matrix, that is, $\mathbf{C}_M = \mathbf{C}_S + \mathbf{C}_R$. Although $\mathbf{C}_R$ is inversely proportional to the ensemble size, it is nonnegligible if the ensemble size is small or moderate, as is the case for most ensemble simulations. Therefore, the conventional EOF modes of the ensemble means (i.e., the eigenvectors of $\mathbf{C}_M$) can be seriously contaminated by the noise. The goal of the MSN EOF analysis is to derive the dominant patterns corresponding to $\mathbf{C}_S$ in the presence of $\mathbf{C}_R$. Its key step is to perform a "prewhitening" transformation with an operator $\mathbf{F}$ so that $\mathbf{F}^T\mathbf{C}_M\mathbf{F} = \mathbf{F}^T\mathbf{C}_S\mathbf{F} + \mathbf{F}^T\mathbf{C}_R\mathbf{F}$, where $\mathbf{F}^T$ is the transpose of $\mathbf{F}$ and $\mathbf{F}^T\mathbf{C}_R\mathbf{F}$ is an identity matrix. After this transformation, the first eigenvector of $\mathbf{F}^T\mathbf{C}_M\mathbf{F}$ maximizes the ratio of the variances of the ensemble mean and within-ensemble deviations and so on. In practice, the prewhitening operator $\mathbf{F}$ can be estimated from the first K-weighted EOF patterns of the intraensemble deviations. A detailed procedure of the MSN EOF analysis is given by Venzke et al. (1999). Applied to the ensemble hindcasts, the leading MSN EOF patterns can be explained as the predictable signals

from all ensemble members. On the other hand, the leading modes of a conventional EOF analysis of the intraensemble deviations can be used to characterize the dominant patterns of the internal noise of the coupled system. The MSN EOF approach has been used effectively in identifying the predictable patterns from ensemble hindcasts by Hu and Huang (2007), Liang et al. (2009), Zuo et al. (2013), Zhu et al. (2015a), and Zhang et al. (2018).

In this study, the MSN EOF analysis is applied to ensembles of hindcasts at every lead month from initial conditions (ICs) of both May and November to examine the seasonal evolution of the predictable patterns and evaluate the limit of predictability. We concentrate on the first two MSN EOF modes because they are statistically significant at the 95% level using the F test (Huang 2004). As a part of the MSN EOF calculation, the EOF modes of the intraensemble variation are also derived (Venzke et al. 1999; Huang 2004). Taking advantage of this by-product, we use the first noise EOF modes to examine the dominant structures of the intraensemble variation at different lead times of the forecast and analyze their potential influences on the corresponding predictable patterns.

In this study, several indices are used to represent major physical processes in the Indo-Pacific region. The ENSO variation is characterized by the SST anomalies averaged over the areas of Niño-3, Niño-3.4, and Niño-4. The WNP-AC index is defined as the SLP anomalies averaged over 120°–160°E, 5°–20°N (Li et al. 2016). The IOD index is defined as the anomalous SST difference between the western equatorial IO (50°–70°E, 10°S–10°N) and the eastern equatorial IO (90°–110°E, 10°S–0°) as in Saji et al. (1999).

3. Prediction skill and predictability

In this section, we evaluate predictive skill of 850-hPa zonal wind over the tropical Indo-Pacific domain in Project Minerva with both May and November ICs. Figure 1 shows correlation skill for 850-hPa zonal wind in Minerva T639 with ICs in May and November for different lead months. Initialized in May, high correlation coefficients (>0.6) are mainly located over the western Pacific warm pool (WP) region in target months of summer (Figs. 1a,b). The regions of significant skill are centered over the IO as well as the central-to-eastern equatorial Pacific in fall (Fig. 1c). Initialized in November, high correlations are located in the equatorial Pacific from fall to spring (Figs. 1c–f). Moreover, the skill is high over the IO in December (Fig. 1d) and rebounds in April (Fig. 1f). The model also shows skill in the western Pacific during winter (Fig. 1e). Overall,
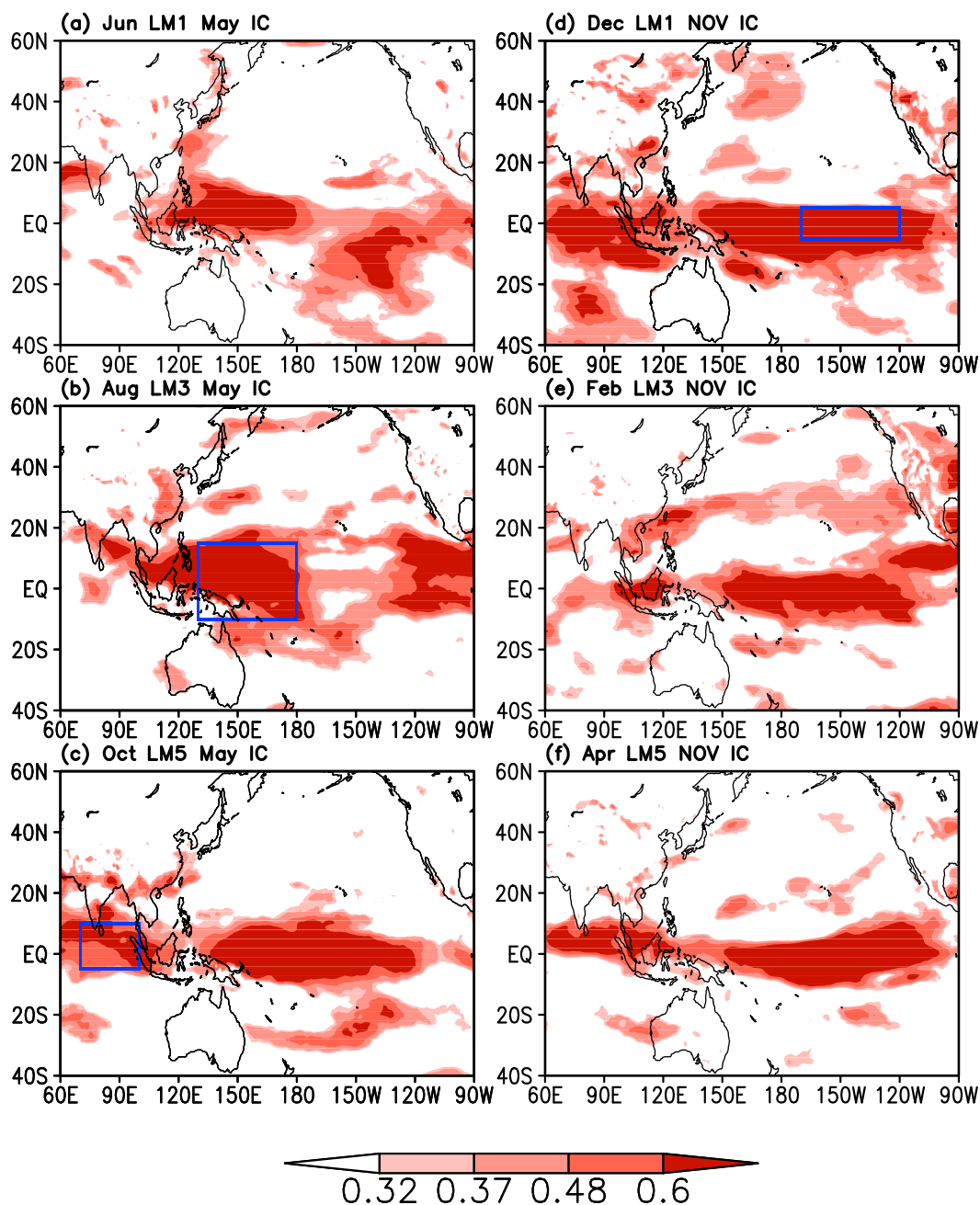
Corr of U850 CFSR&MINERVA

FIG. 1. Correlations between observed 850-hPa zonal wind (m s^{-1}) and predicted 850-hPa zonal wind (m s^{-1}) in T639 with ICs in (a)–(c) May and (d)–(f) November for different lead months. Values exceeding the 90% (0.32), 95% (0.37), and 99% (0.48) confidence levels are shown. The blue boxes in (b), (c), and (d) denote the high correlation areas of the WP, IO, and Niño-3.4 regions, respectively.

skillful regions migrate seasonally and are concentrated in the tropical Indo-Pacific Ocean.

To analyze the comprehensive prediction skill of the 850-hPa zonal wind associated with the major modes

of variability in the tropical Indo-Pacific domain, the correlation coefficients and root-mean-square error (RMSE) of area-averaged indices over three high-skill areas (Niño-3.4, WP, and IO regions; blue boxes in
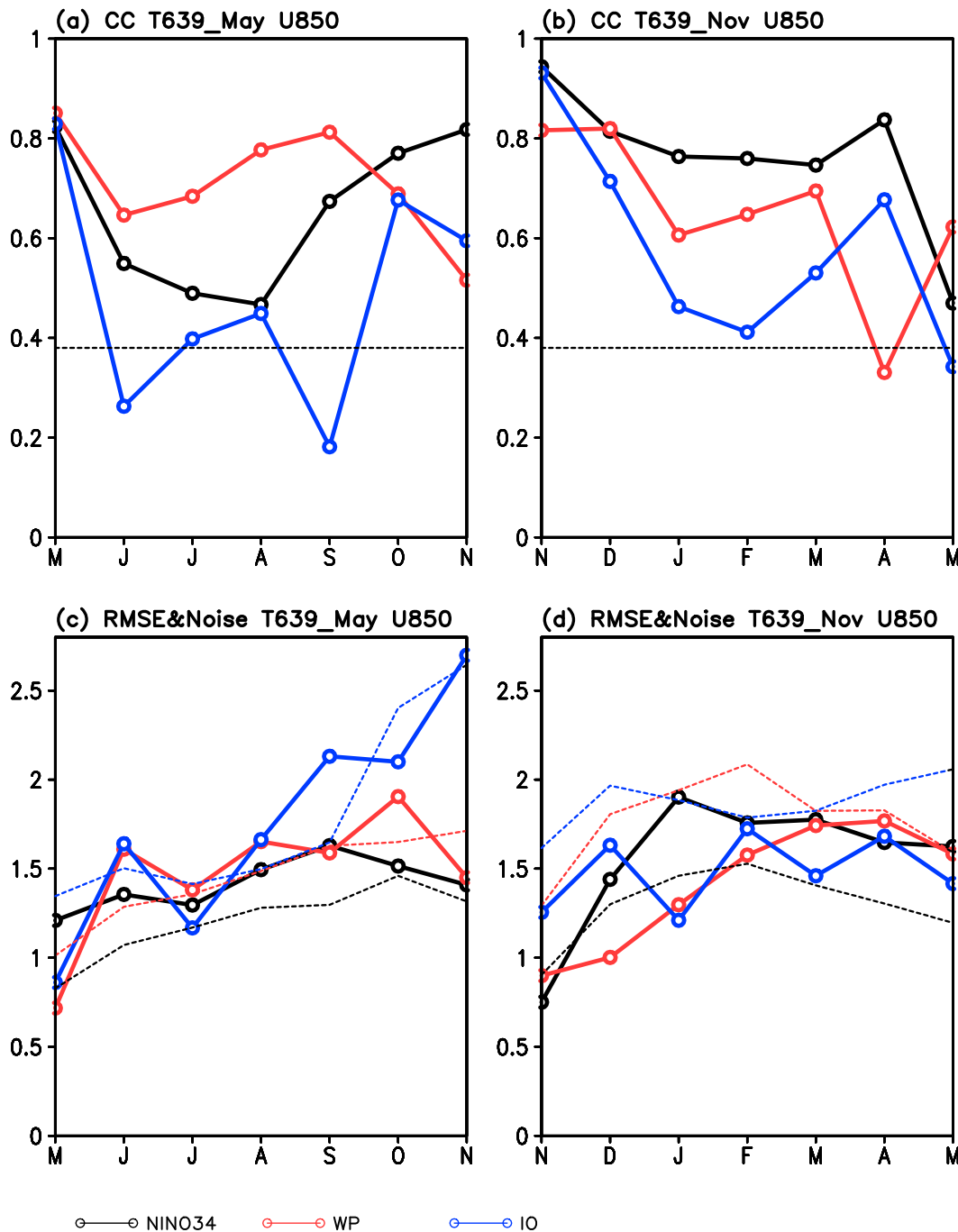
FIG. 2. (a),(b) Coefficients of correlation and (c),(d) RMSE between observation and ensemble mean hindcast with (left) May ICs and (right) November ICs in different lead months for area-averaged 850-hPa zonal wind (m s^{-1}) of the Niño-3.4 (black solid line), WP (red solid line), and IO regions (blue solid line). The dashed lines in (a) and (b) denote the 95% confidence level. The black, red, and blue dashed lines in (c) and (d) denote the intraensemble spread for the Niño-3.4, WP, and IO regions, respectively. The x coordinate indicates the corresponding lead months.

Fig. 1) are calculated (Fig. 2). The correlation coefficients for the Niño-3.4 region (black curves, Fig. 2) are significant in all lead months with both May and November ICs, but show a valley during target months of summer, possibly attributed to the spring predictability barrier (e.g., Webster and Yang 1992; Figs. 2a,b). The correlation skill for the WP region, however, is generally higher than the Niño-3.4 U850 index during summer and

fall, though decreasing faster during spring (Figs. 2a,b). In comparison, the correlation skill of the IO region is lower than the other two, but rebounds in October (April) with May (November) ICs (Figs. 2a,b). The RMSE, on the other hand, does not show large differences among the three regions (Figs. 2c,d). For May ICs, the RMSE for both the Niño-3.4 and WP regions are approximately 1.5 for all lead months (Fig. 2c). The RMSE for the IO region is higher than the RMSEs for the former two regions after 3-month lead (Fig. 2c). For November ICs, the RMSE shows a rapid (slower) increase from 0-month lead to 2-month (4 month) lead for the Niño-3.4 (WP) region (Fig. 2d). The RMSE for the IO region, however, does not show obvious increase with the lead time (Fig. 2d). The intraensemble spread for the WP and IO regions almost matches the RMSE with May ICs, suggesting a reasonably decent reliability (Figs. 2c,d; Johnson and Bowler 2009). However, the ensemble spreads are generally larger than the RMSE (over spread) with November ICs (Fig. 2d). On the other hand, there are obviously smaller intraensemble spreads for Niño-3.4 region with both ICs, contributing to under dispersion for this region, suggesting that the model is somehow overconfident in ENSO prediction, which is quite common in the current forecast systems (Figs. 2c,d; Zhu et al. 2013).

Going beyond the deterministic metrics, we examine the signal-to-noise ratio of 850-hPa zonal wind predictions as a function of lead time (Fig. 3). Following Rowell et al. (1995), the signal-to-noise ratio is defined as the ratio between interannual standard deviation of ensemble mean and the standard deviation of the intraensemble variations, which measures the predictability of the coupled system. The maximum signal-to-noise ratio is mainly located over the equatorial Pacific, with the center in the western Pacific during summer and fall seasons, and it shifts eastward to the eastern-central Pacific during winter and spring, demonstrating a higher predictability of 850-hPa zonal wind over the equatorial Pacific (Fig. 3). There are secondary maximum centers over the IO and WNP regions during fall–winter and winter–summer, respectively (Fig. 3). However, the ratio is generally smaller than 1.0 over these two regions, except in target month of December, indicating relatively lower predictability of 850-hPa zonal wind over the IO and WNP regions.

4. Seasonal evolution of the predictable patterns

Studies have demonstrated that the major climatological features over the Indo-Pacific region are well predicted in the Minerva hindcasts (Zhu et al. 2015b; Manganello et al. 2016). Although seasonal predictions

of ENSO and tropical cyclone activity in the Minerva hindcasts have been evaluated, no investigation of the predictable patterns of the atmospheric low-level circulation, and their seasonal dependence, over the tropical region in these hindcasts has been done so far and is presented in this section.

a. Predictable ENSO patterns

In this subsection, we depict the predictable patterns of 850-hPa zonal wind associated with ENSO using the ICs in May and November. Figure 4 shows the first MSN EOF modes (the most predictable patterns) of 850-hPa zonal wind over the Indo-Pacific region in different lead months for T639 with ICs in May. The spatial patterns of MSN EOF1 with different lead times show similar features, characterized by anomalous westerlies over the central-eastern equatorial Pacific (Fig. 4, left). Although the westerly wind anomalies are quite steady in different seasons/lead months, the zonal wind anomalies over the IO show substantial monthly variation. At LM0 (target month of May), the anomalous easterlies are over the IO north of the equator (0°–15°N; Fig. 4a). The center of easterly loadings shifts to the equatorial IO, but is generally weak during the target months in summer (Figs. 4c,e,g). The equatorial easterlies strengthen during the fall months in the IO as the equatorial westerly wind in the central Pacific also peaks (Figs. 4i,k,m). It should be noted that a particular phase (El Niño) is chosen to be shown for the MSN EOF pattern but it could be equally well applied to opposite phase (La Niña). These MSN EOF patterns are apparently ENSO related because their MSN first principal components (PC1s) show large similarities among different lead months and with almost the same peaks and valleys that correspond to the El Niño and La Niña years (e.g., 1997 and 1999; Fig. 4, right). The percentages of explained variance are above 36.2% for all leads.

To evaluate the prediction skill of these predictable patterns identified by the MSN EOF, observations are projected onto the first MSN EOF modes, and correlations between the MSN PC1s and their corresponding projected observational PC1s are calculated. These correlation coefficients exceed the 99% confidence level of the t test (0.48) for all lead months (see the values of R in Fig. 4, right), with a valley in the target months of summer (LM1–LM3). Furthermore, each of the individual ensemble members is projected onto the first MSN EOF modes. The average correlation coefficients between the MSN PC1s and the projected PC1s for ensemble members exceed the 99% confidence level of the t test for all leads and do not obviously decrease with the increase in lead time except from LM0 to LM1 (see
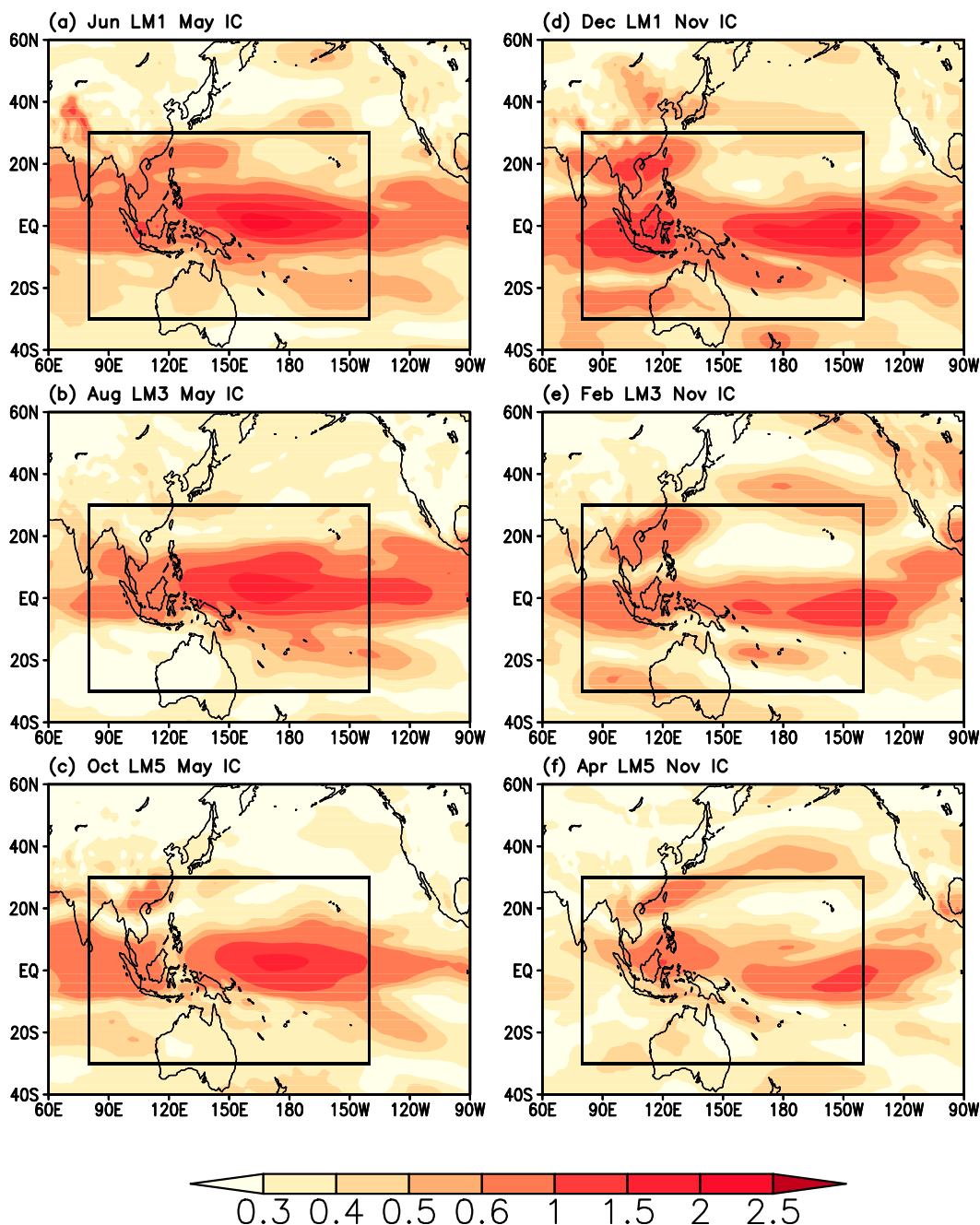
Signal to Noise Ratio for U850

FIG. 3. Signal-to-noise ratio for 850-hPa zonal wind with (a)–(c) May ICs and (d)–(f) November ICs in different lead months. The black box denotes the area for MSN EOF.

values of R1 in Fig. 4, right). The large percentage of explained variance and statistically significant correlations of MSN PC1s with the projected PC1s for observation and for ensemble members indicate the high predictability of these patterns.

We further investigate the ocean–atmosphere anomalies that are associated with the most predictable patterns of 850-hPa zonal wind. In Fig. 5, the correlation for SLP and precipitation anomalies and the regression patterns for 850-hPa wind and SST from LM0 to LM6
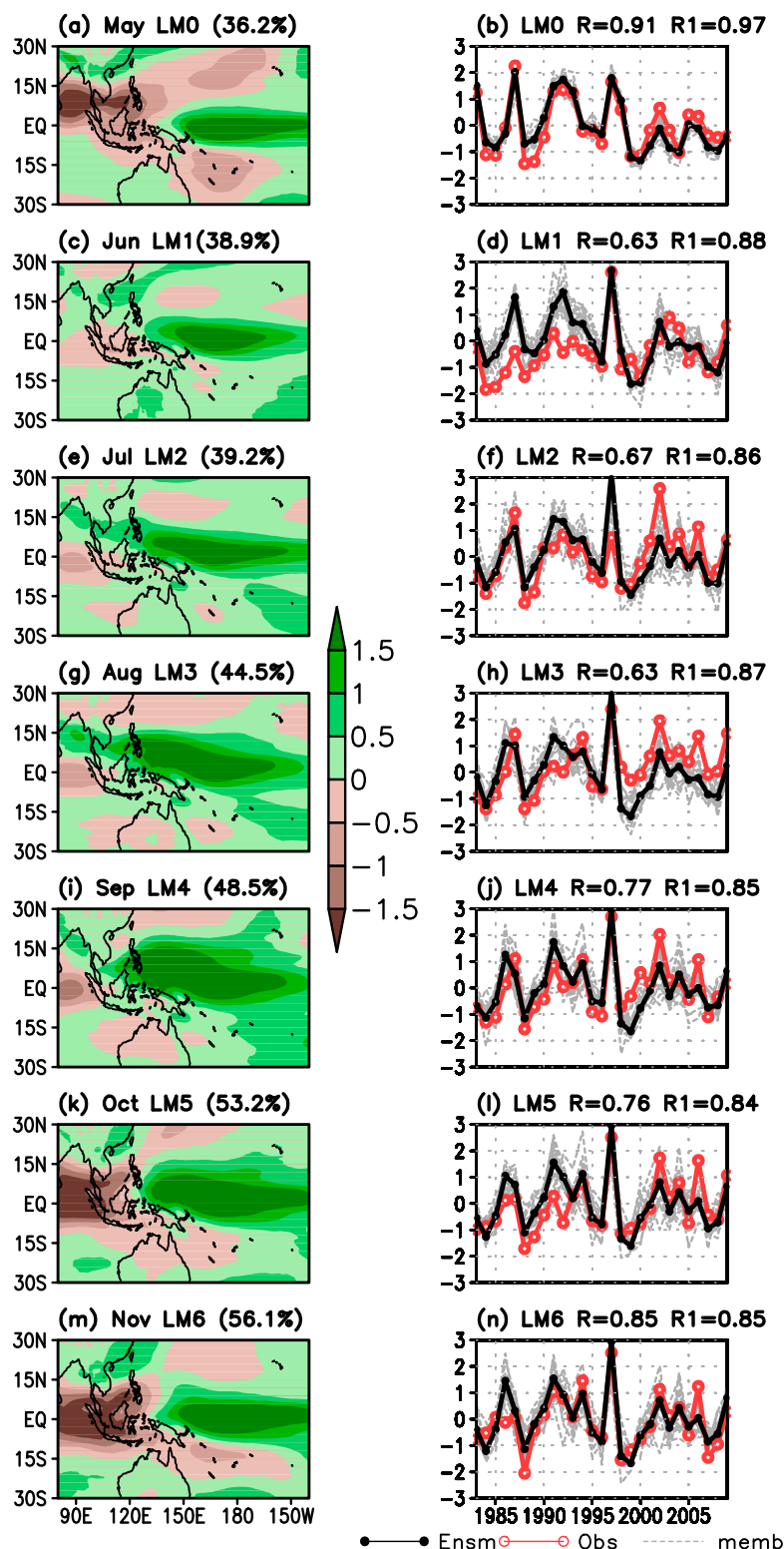
FIG. 4. The first MSN EOF modes of 850-hPa zonal wind (m s^{-1}) in different lead months for T639 with ICs in May. (left) The spatial patterns. (right) The solid black lines are the PCs of ensemble means, and the solid red lines and dashed black lines represent the PCs that are computed by projecting the 850-hPa zonal winds in observation and ensemble members upon the MSN EOF1, respectively. The R value represents the correlation coefficient between the ensemble mean PC and projected observational PC, and R1 represents the averaged correlation coefficient between the ensemble mean PC and projected PCs for individual members.
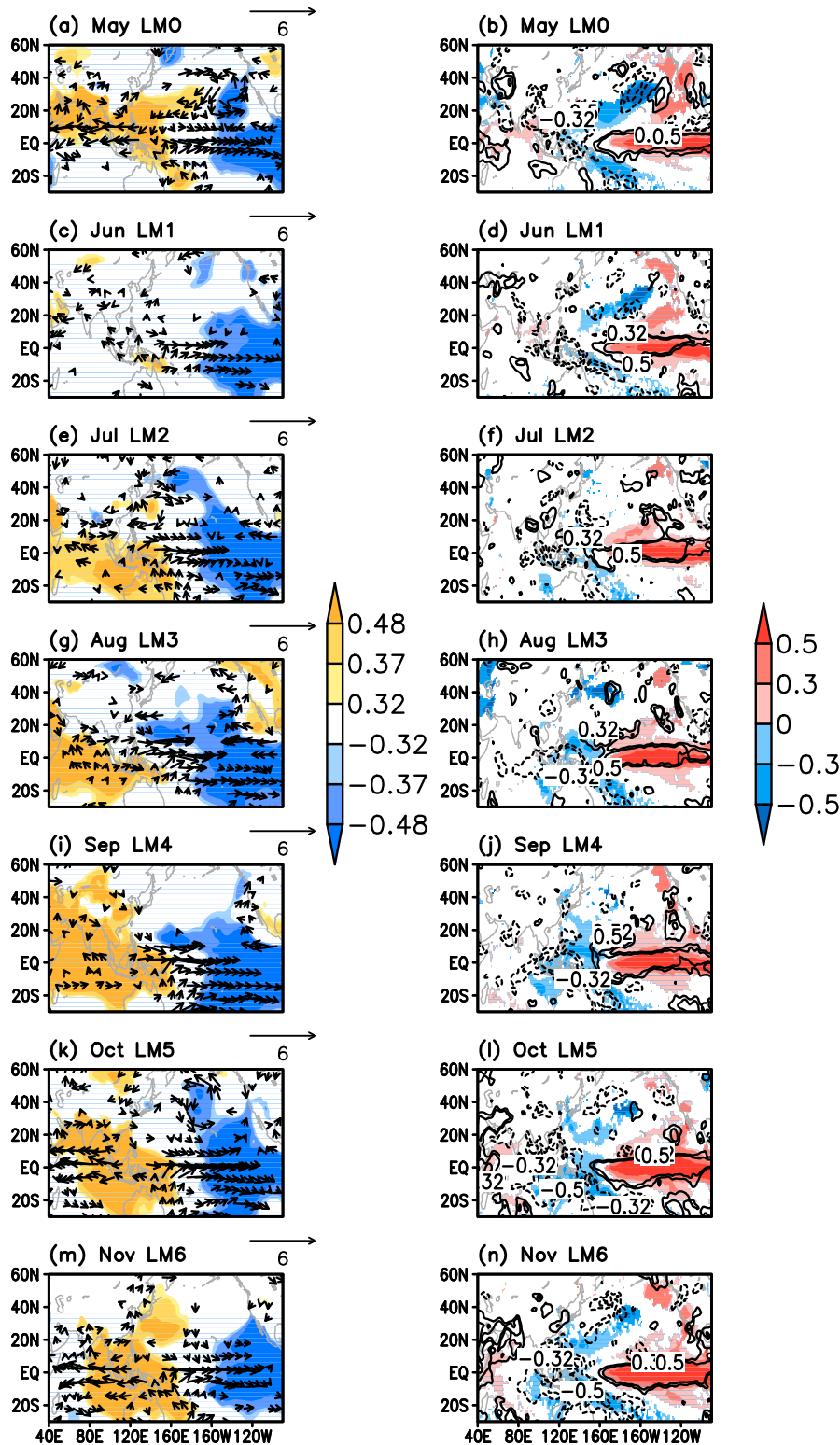
FIG. 5. Correlations of observed SLP and rainfall with ensemble mean PC1s and regression of observed 850-hPa wind (m s^{-1}) and SST (K) against ensemble mean PC1s in different lead months for T639 with ICs in May. The (left) patterns for SLP (shading) and 850-hPa wind (vectors), and (right) patterns for SST (shading) and rainfall (contours). Only values exceeding the 90% confidence level are shown.

(i.e., target months of May–November) show the features corresponding to seasonal evolution of ENSO development. Note that the anomalous low-level wind over the northern IO in the target month of May demonstrates a weak or delayed onset of Asian monsoon as the El Niño event is initiated. However, this ENSO–monsoon relationship is weakened as the predicted equatorial westerlies in the Pacific are extended into the target months of summer (Figs. 5a,c,e,g). The wind signals over the equatorial IO strengthen during the target months of fall season as the ENSO signals enhance in the Pacific (Figs. 5i,k,m). The SST and precipitation patterns in this season (Figs. 5l,n) show a typical IOD structure (Saji et al. 1999), suggesting an ENSO–IOD connection in this season (e.g., Huang and Kinter 2002; Luo et al. 2010; Stuecker et al. 2017). The close relationships between ENSO and the first modes of MSN EOF for May ICs are also identified by the significant correlations between observed (model) ENSO indices and MSN PC1s, as shown in Fig. 6a (figure not shown). A dip of the Niño-3 correlation in summer (LM2–LM4) is consistent with Barnston et al. (2012, their Fig. 1), which is generally considered as the consequence of ENSO spring predictability barrier (e.g., Barnston et al. 2012; Tippett et al. 2012; Barnston and Tippett 2013; Zhang et al. 2018). The high correlations with the IOD index during LM4–LM6 (September–November) can be seen in Fig. 6b. A high prediction skill of the IOD in the ECMWF System 3 during October–December is shown by Shi et al. (2012). The MSN EOF2, to be discussed in detail in section 4, is not significantly correlated with the contemporary ENSO indices (Fig. 6c). Actually, there are large similarities between correlations of the MSN PCs with the model indices (figure not shown) and observed indices (Fig. 6), indicating the PCs represent these phenomena correctly.

For November ICs with target months from late fall to late spring, the most predictable patterns also show ENSO features, which are well predicted by the model for all leads (Figs. 7 and 8). Consistently, the MSN PC1s are significantly correlated with ENSO indices, with correlation coefficients above 0.8 in the first four months of the hindcast (Fig. 6b). The reduction of correlation afterward again signifies the spring barrier. The correlations of the MSN PC1s with the WNP-AC/IOD indices for May and November ICs show a phase locking of the WNP-AC/IOD to the annual cycle of ENSO (Figs. 6b,f). Beside the first MSN EOF modes, the second MSN EOF modes (the second most predictable patterns) with November ICs are also closely linked to ENSO, but only for the decaying phase of ENSO. Interestingly, the monthly evolution of the second predictable patterns is also ENSO related, characterized by a southward shift

of anomalous westerly wind, the so-called combination mode that plays an important role in the termination of strong El Niño event (Fig. 9; Stuecker et al. 2013, 2015). Correspondingly, the MSN PC2s are significantly correlated with Niño-4 indices especially for the spring months, but are insignificantly correlated with Niño-3 and Niño-3.4 indices (Fig. 6g), because of the decaying of SST anomalies over the eastern equatorial Pacific during the post-ENSO spring. These features depicted above are consistent with those in Zhang et al. (2018), indicating that the most predictable ENSO patterns are not sensitive to the forecast system used.

b. Predictable WNP patterns

The second MSN EOF modes of 850-hPa zonal wind in different lead months for T639 with May ICs are shown in Fig. 10. The percentage values of variance explained by these MSN EOF2s are 20.2, 18.5, 21.0, 16.2, 12.9, 9.5, and 11.5 for LM0, LM1, LM2, LM3, LM4, LM5, and LM6, respectively. The predictable signals are mainly located over the WNP. At LM0, the easterly wind anomalies are centered east of the Philippines between the equator and 15°N (Fig. 10a). This wind band shows a northward shift in the target months of summer from June (Fig. 10c) with its center reaching 15°N in September (Fig. 10i); then, it shows a southward shift in the target months of fall (Figs. 10k,m). There are also some signals over the IO in the target months of May and November (Fig. 10, left). To link the wind patterns to regional climate variation, we calculate correlations of the MSN PC2s with the WNP-AC and IOD indices. The results show that these predictable patterns are mainly associated with the WNP-AC rather than the IOD in summer and fall months (Fig. 6d). The second modes of MSN EOF are well predicted by the hindcasts of Project Minerva with T639 resolution for all lead months (see the values of R in Fig. 10, right), though the prediction skill is lower than those for the first MSN EOF modes. Unlike those for the MSN PC1s, the spread among ensemble members increases rapidly from the target months of late spring to fall (see values of R1 in Fig. 10, right), suggesting lower predictability of the second most predictable patterns.

Correlation and regression patterns for ensemble mean PC2s of different lead months with May ICs are shown in Fig. 11. In the target month of May, the associated patterns show weak ENSO features, consistent with the insignificant correlations between the MSN PC2 and ENSO indices (Figs. 11a,b and 6c). An anomalous anticyclonic circulation appears over the WNP in June, associated with positive SLP and negative SST over the region, together with a decrease in rainfall east of the Philippines and an increase in rainfall southeast of
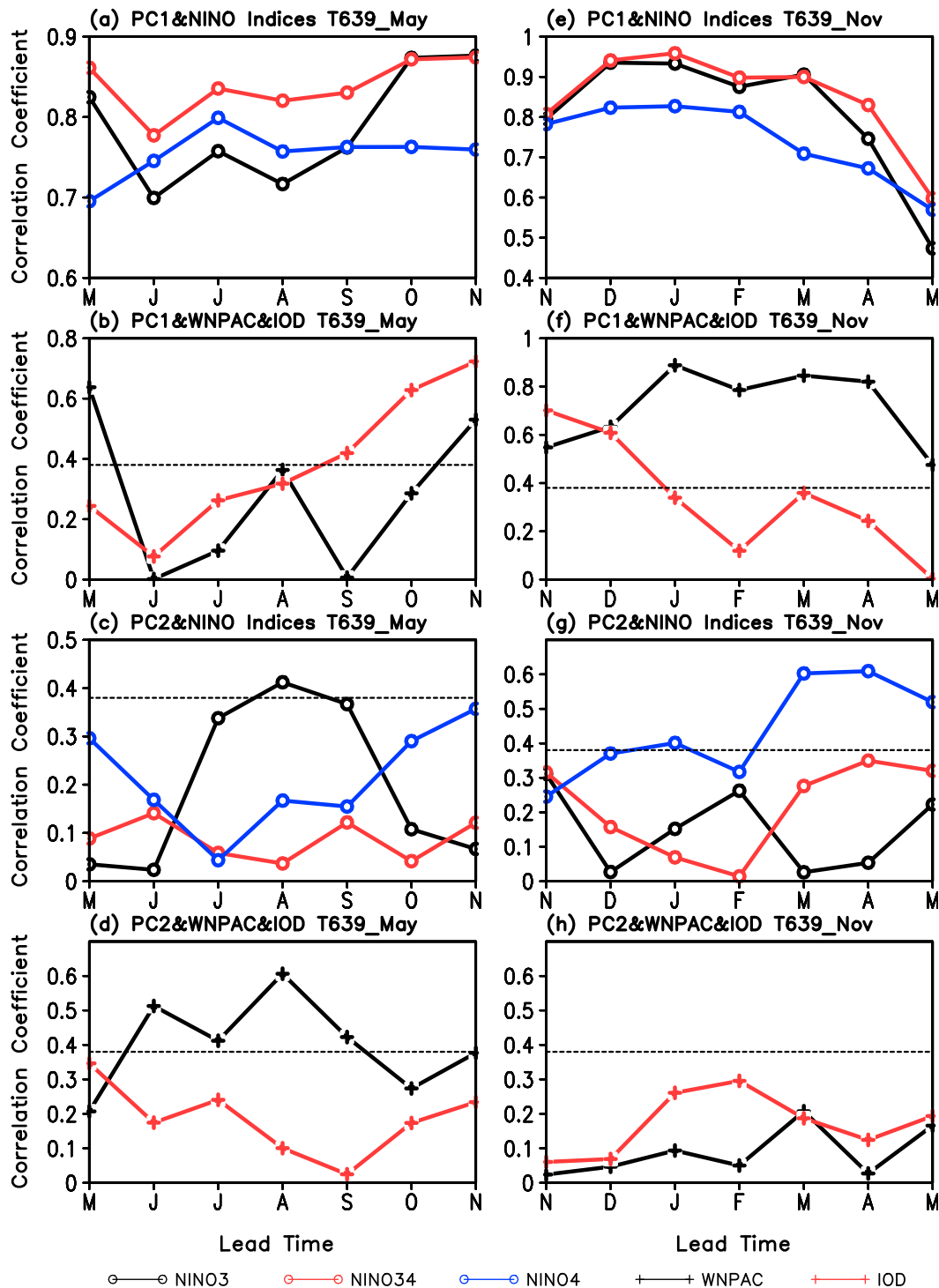
FIG. 6. Correlation coefficients between observed (a),(e) Niño-3/Niño-3.4/Niño-4 index and ensemble mean PC1; (b),(f) WNP-AC/IOD index and ensemble mean PC1; (c),(g) Niño-3/Niño-3.4/Niño-4 index and ensemble mean PC2; and (d),(h) WNP-AC/IOD index and ensemble mean PC2. The left (right) panels show the correlation coefficients for T639 with ICs in May (November). The x coordinate indicates the corresponding lead months. Horizontal dotted lines denote the 95% confidence level.
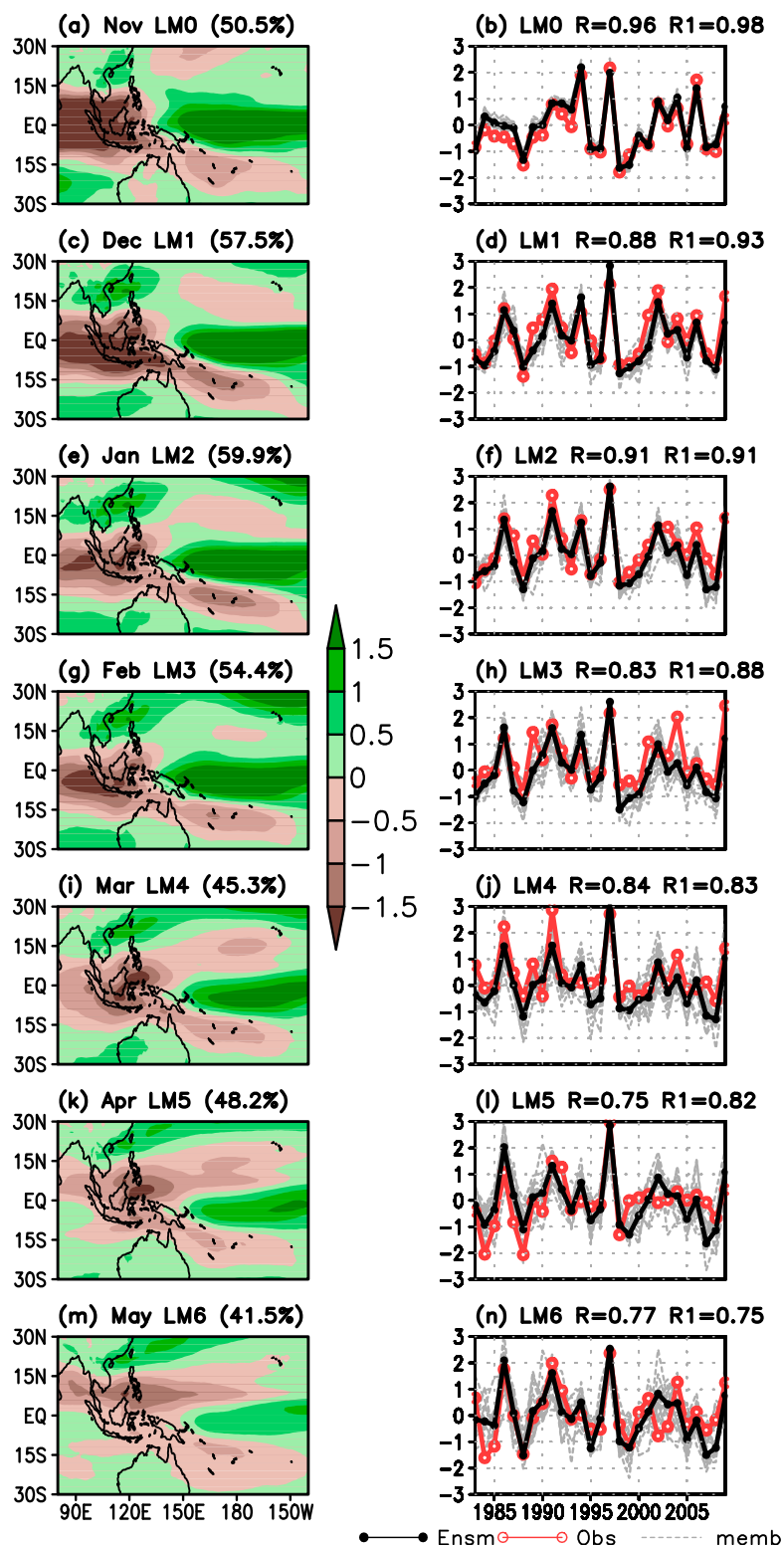
FIG. 7. As in Fig. 4, but for November ICs.
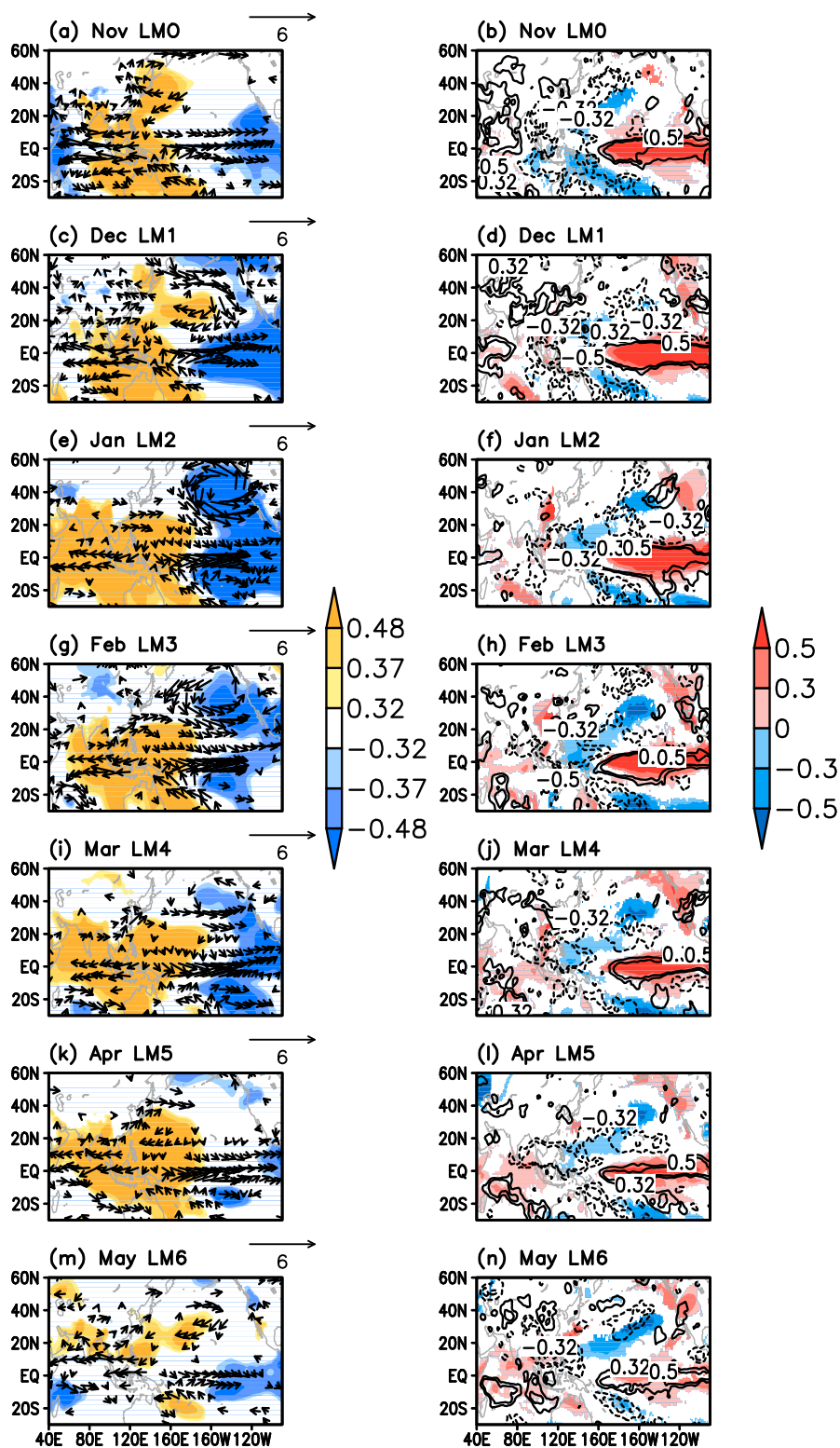
FIG. 8. As in Fig. 5, but for November ICs.
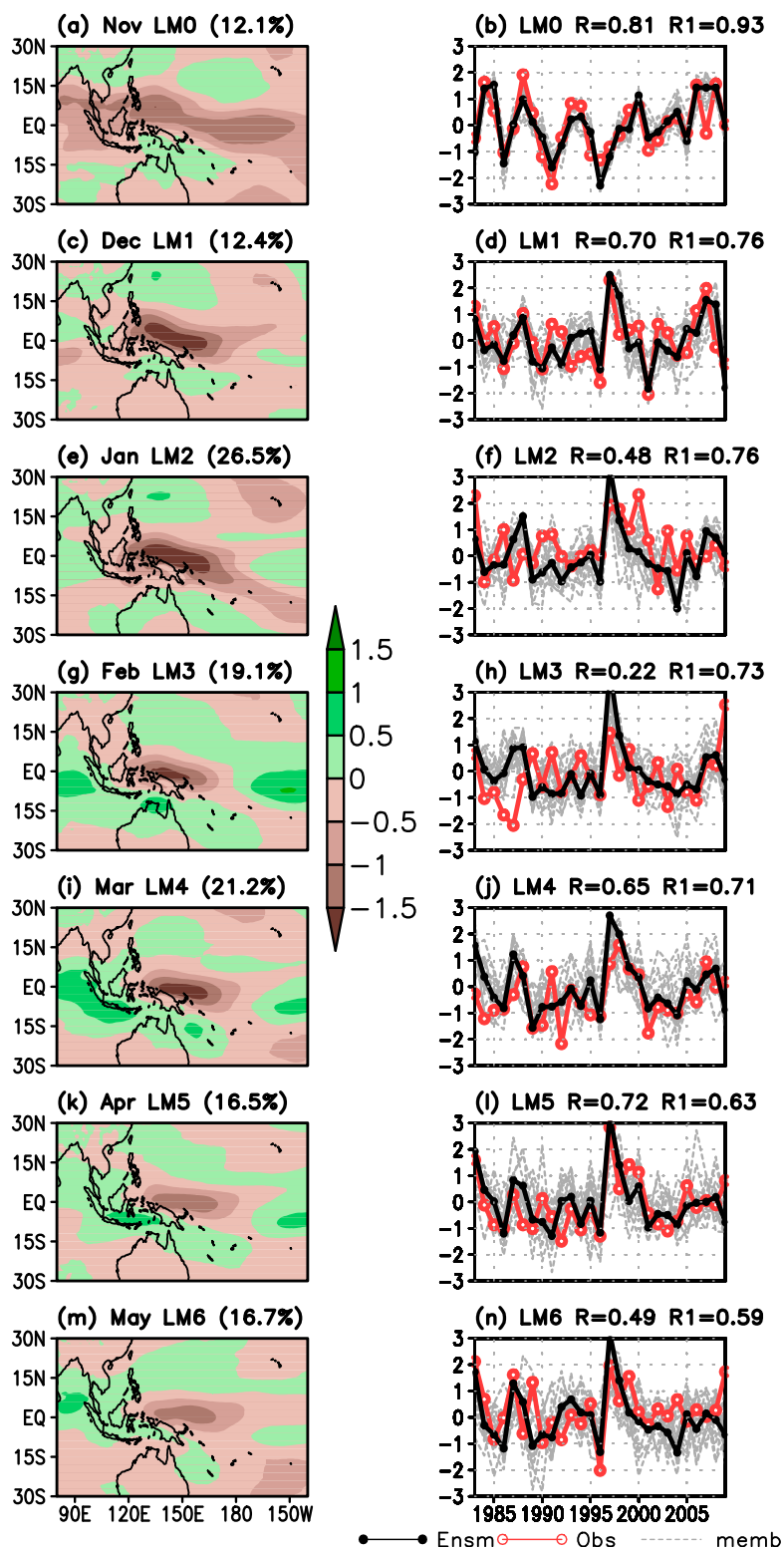
FIG. 9. As in Fig. 7, but for the second modes.
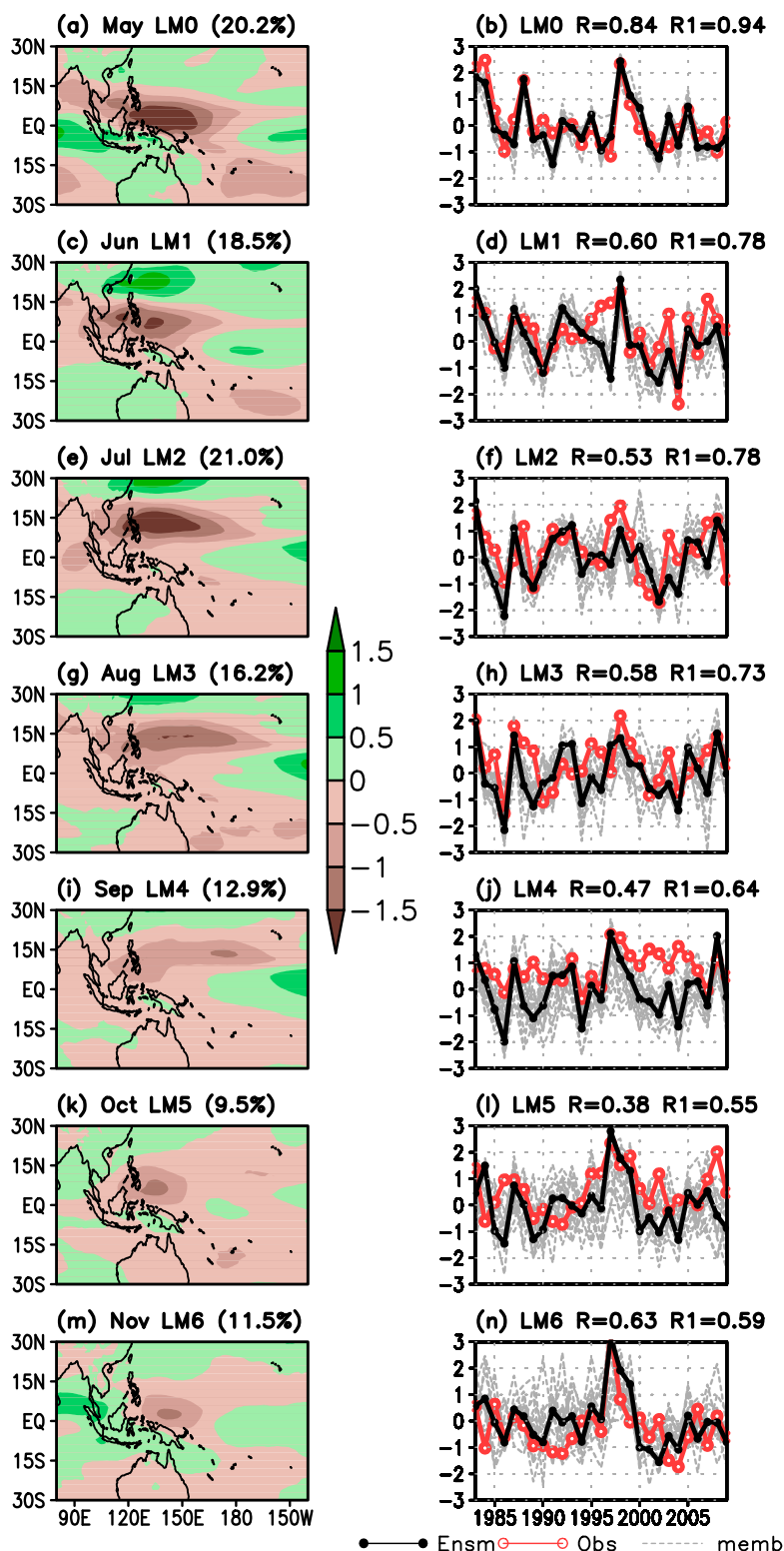
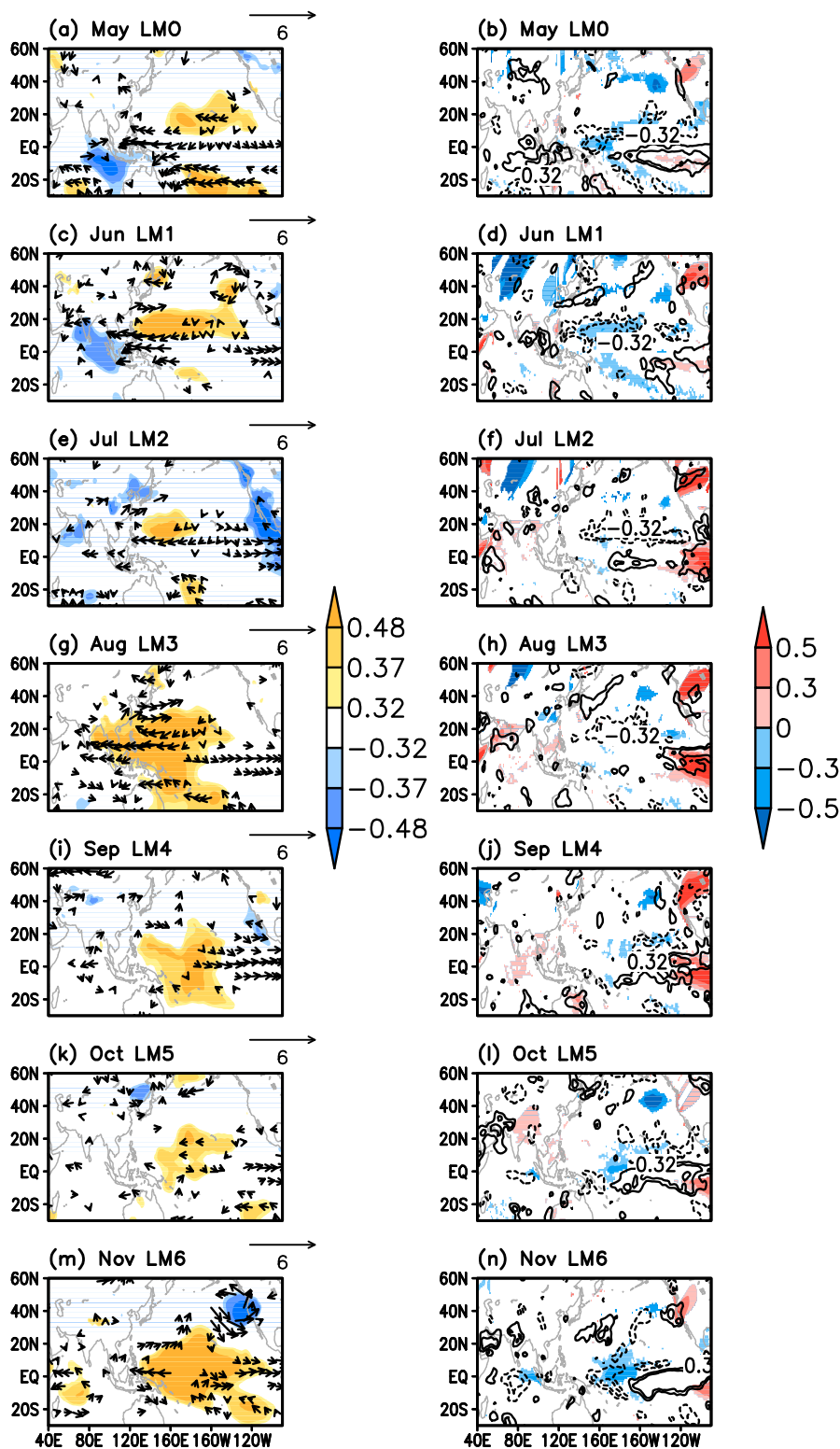FIG. 10. As in Fig. 4, but for the second MSN EOF modes.

FIG. 11. As in Fig. 5, but for the ensemble mean PC2.

Japan (WNP monsoon features). This WNP-AC shows a northward shift during the summer months and then shifts southward in the fall months, associated with the lifespan of the WNP monsoon (Fig. 11).

In addition, the hindcasts made using the T319 configuration were examined to evaluate the resolution effect. Generally, the results in T319 hindcasts are similar to those in T639 hindcasts (figure not shown). However, the MSN PC2 in October with November ICs is significantly (insignificantly) correlated with the WNP-AC index and the IOD index in October for T319 (T639). The correlation coefficients of the MSN PC2 with the WNP-AC index and the IOD index in October for T319 are 0.44 and 0.40, respectively. These features suggest that the effect of atmospheric horizontal resolution is small, especially for the predictable ENSO patterns. However, the atmospheric horizontal resolution may have some influences on the predictable patterns during the fall season when both the WNP-AC and the IOD are well developed.

5. Intraensemble variability

Here, we examine the intraensemble variability of 850-hPa zonal wind within the tropical Indo-Pacific region using Project Minerva hindcasts to identify the most likely disrupters of seasonal predictions. The first noise EOF modes for both May and November ICs in T639 are analyzed. Interestingly, the leading EOF modes of the intraensemble variability show coherent structures as a function of lead month, implying a month-to-month evolution of the intraensemble spread driven by model dynamics. The evolution also shows distinct characteristics during summer–fall and in winter–spring.

a. Summer–fall evolution

Figure 12 shows the first EOF modes of model noise data for 850-hPa zonal wind from the target months from May to November with May ICs for T639. In late spring, the large model spread is mainly located south of 15°S to the east of Australia (Fig. 12a), which likely originates from the southern extratropics. During the boreal summer months, while the spread in the south persists, the location of large model spread also appears to the north of the equator. Its structure shows westerly (easterly) wind anomalies from north of the equator to about 15°N extending from the IO to the WNP region, with easterly (westerly) wind anomalies further to the north (Figs. 12c,e,g). Their spatial structures are similar to the spatial patterns of the second MSN EOF modes (Figs. 10c,e,g). For the boreal fall months, the spatial structures of first EOF modes of model noise data

(Figs. 12k,m) show zonal wind anomalies of opposite signs between the equatorial Pacific and IO, which resemble the first predictable patterns in these months (Figs. 4k,m). The noise PC1s are demonstrated on the right-hand side of Fig. 12 as the projection of ensemble members onto the noise EOF modes (thin black curves). The temporal variation of the noise level is represented by the standard deviation of the ensemble members (red curve), which shows weak interannual variation in late spring and summer, but displays strong interannual variation in the boreal fall months (red line in Fig. 12, right). In particular, the results for the early to mid-1990s and 2000s show relatively high noise level for ENSO-like variability (Figs. 12l,n). It is interesting to note that these were relatively weak but broad warm episodes in the tropical Pacific (see Fig. 4, right, for example).

To find the mechanisms associated with the intra-ensemble variability for May ICs, we calculate correlations of noise SLP and rainfall with noise PC1s and regressions of 850-hPa wind and SST against noise PC1s of different lead months for T639 (Fig. 13). The patterns for May and June (Figs. 13a–d) are less organized than those in the later months. However, a noticeable feature in May is strong negative SLP anomalies with an anomalous cyclonic circulation south of 20°S to the east of Australia, which seems to have an extratropical origin (Fig. 13a). This extratropical perturbation persists in June and expands northward mainly along the eastern boundary of the Pacific (Fig. 13c), which is similar to the extension route described in Huang and Shukla (2008), albeit for a different season. On the other hand, another low SLP anomaly with a cyclonic circulation appears in the WNP region with its center near the Philippines around 20°N between 120°E and the date line in June. In July, the WNP cyclone becomes more dominant than the southern extratropical perturbations (Fig. 13e) and shows a wave train similar to the PJ–IO pattern (e.g., Kosaka et al. 2013), with upstream positive SLP anomalies expanding from the IO into the Maritime Continent and a downstream wave train through Japan. Interestingly, this feature is associated with mild cold SST anomalies extending from the northern IO to the WNP (Fig. 13f), suggesting a connection to the Indian Ocean Basin mode (IOB). The precipitation is generally reduced under the anticyclonic circulation over the IO but increased in the cyclonic circulation over the WNP. As a result, precipitation is enhanced over cold SST anomalies in the WNP. To substantiate the connection of the northwestern Pacific noise pattern with the rest of the basin, we have calculated the EOF of noise SLP and correlated the PCs of the leading modes with noise SST and SLP
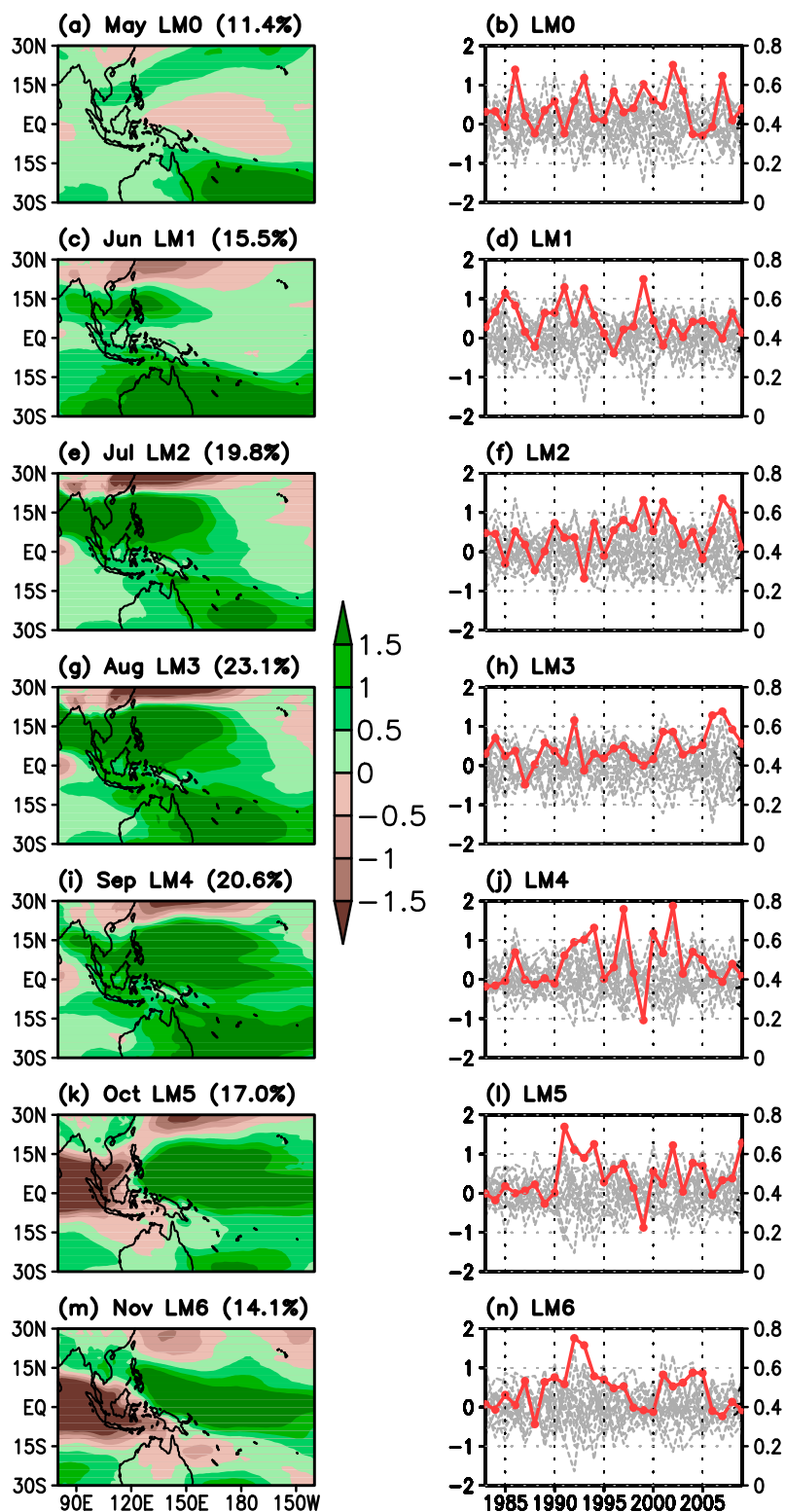
FIG. 12. The first EOF modes of model noise data for 850-hPa zonal wind (m s^{-1}) in different lead months for T639 with ICs in May. (right) The dashed black lines represent the corresponding PCs for ensemble members, and the red line represents the standard deviation of the ensemble members.
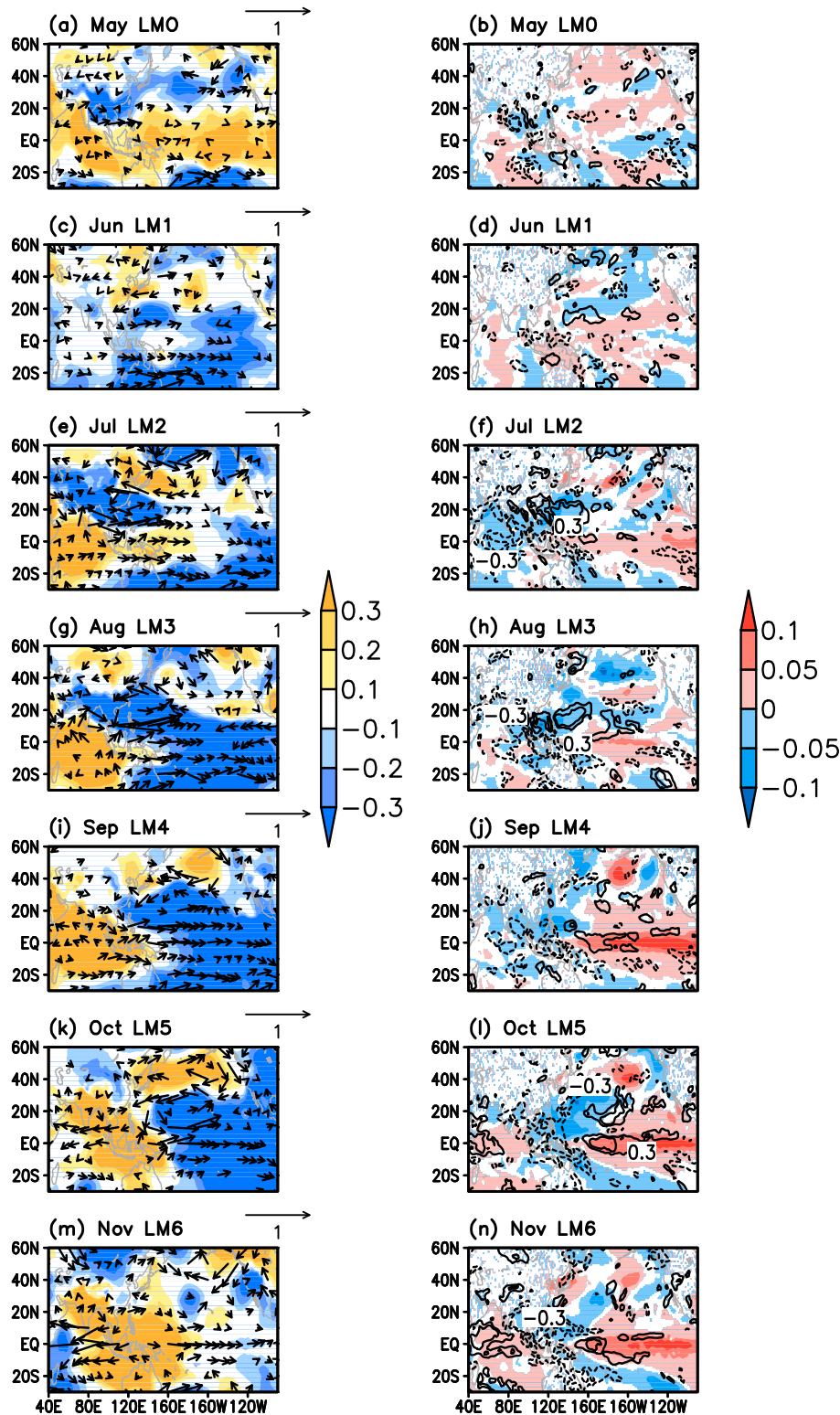
FIG. 13. Correlations of noise SLP and rainfall with noise PC1s and regression of noise 850-hPa wind (m s^{-1}) and SST (K) against noise PC1s in different lead months for T639 with ICs in May. (left) The patterns for SLP (shading) and 850-hPa wind (vectors) and (right) the patterns for SST (shading) and rainfall (contours). Only values exceeding the 95% confidence level are shown.

(figures not shown). Both the PJ–IO pattern and IOB appear in the correlation patterns, verifying the connection between the WNP noise pattern and the IO region. By August, the spatial structure is further consolidated into a tropical mode dominated by an anomalous anticyclone (high SLP) over the IO and a cyclone (low SLP) over the WNP. This pattern implies a direct thermal cell connecting its uplifting branch over the WNP with subsidence over the eastern IO, as described in Huang and Shukla (2007), which is sustained through September and October (Figs. 13i,k). Our results are also consistent with the recent findings by Ma et al. (2017a).

During the boreal fall months, the intraensemble spread of 850-hPa zonal wind is also characterized by the opposite wind anomalies in the equatorial Pacific and the IO, which are mainly associated with the SST anomalies over the central-eastern equatorial Pacific, the Walker circulation (Figs. 13i–n). Huang and Shukla (2007) suggested that the WNP-IO variation described above can trigger the equatorial wind anomalies in the central Pacific during the boreal fall season. Once generated, the equatorial wind anomalies seem to evolve via the ENSO-like coupled dynamics (Larson and Kirtman 2015). These correlation and regression patterns are similar to those for the first MSN EOF modes during the boreal fall season, suggesting that the prediction spread over this region results mainly from the internal uncertainty of the model. This is different from Larson and Kirtman (2017), which stated that the uncertainty of ENSO prediction is mainly from the equatorial wind perturbations in March.

The resemblance in the spatial structures between the predictable and noise patterns suggests that the noise growth may be driven by the same dynamics as that for the predictable signals and that such noise-induced feedback generates the difference in the evolution of the predictable signals among ensemble members (Figs. 4, 10, and 12). To further clarify this issue, Fig. 14 shows composite differences in ensemble mean SST and 850-hPa wind between large positive ($>$1.0) and negative (<-1.0) values of MSN PC1 and composite of noise SST and 850-hPa zonal wind magnitude for large positive values ($>$1.0) of MSN PC1 with May ICs in different leads. The noise magnitude is defined as the standard deviation among the ensemble members. As expected, there are large similarities between these composite figures and correlation (regression) figures for ensemble mean; both show ENSO developing features (Figs. 14, 4, and 5, left). Large spread appears over the extratropical Northern Hemisphere in all leads, consistent with the leading noise EOF modes (Fig. 14, right). More importantly, with hindcasts initialized in May, the spread of wind noise over the tropics is small in the target month

of June. A large spread first appears over the WNP in August and then in the equatorial Indo-western Pacific, as shown by the contour of $2\,\mathrm{m\,s}^{-1}$. This is largely consistent with the noise EOF patterns in these months (Figs. 12g,k). The corresponding SST magnitudes are also similar to correlation (regression) figures for ensemble spread (as shown in Figs. 13h,l). Composites for the positive and negative ENSO events bear strong resemblance to Fig. 14 (figure not shown). Overall, these composites are consistent with the noise patterns depicted with the EOF analysis, further demonstrating the relationship between the predictable signals and noise, that is, at relatively long leads, the noise distribution in the tropics reflects the different growths of the predictable patterns due to the different amplification of the initial differences. The reason for this geographic distribution is due to the coupled instability, through which the initial differences generate lasting influences on the predictable signal (e.g., Larson and Kirtman 2017).

b. Winter–spring evolution

Figure 15 shows the first noise EOF modes for November ICs. At LM0, the largest model spread is mainly located over the extratropical Northern Hemisphere, with westerly (easterly) wind anomalies north of 15°N and weaker easterly (westerly) wind anomalies farther south (Fig. 15a). The westerly (easterly) wind anomalies expand southward over the western Pacific in the next two months (Figs. 15c,e,g), which trigger westerly (easterly) wind anomalies over the central equatorial Pacific and easterly wind anomalies over the equatorial IO in February (Fig. 15g). During the boreal spring season, the equatorial zonal wind anomalies are enhanced (Figs. 15i,k,m). It should be noted that the sign does not matter for the spread EOFs; the spatial structures of these ensemble spreads tell their origins. The time series and their standard deviations show that the spread level is generally uniform throughout the period (Fig. 15, right).

Figure 16 shows the correlations (regressions) of noise SLP/rainfall (850-hPa wind/SST) with (against) noise PC1s of different lead months for T639 with November ICs. The most striking feature is the dipole SLP pattern over the North Pacific from November to the following March, which bears a strong resemblance to the North Pacific Oscillation (NPO; Rogers 1981). There is a strong anomalous cyclonic circulation over the southern lobe of this dipole. The SLP anomalies first expand southwestward in November and December (Figs. 16a,c). Trade winds weaken throughout the subtropics when low pressure occupies the southern lobe of the NPO, reducing the upward surface latent heat flux (SLHF) and thus warming the underlying ocean (Figs. 16a–d). The

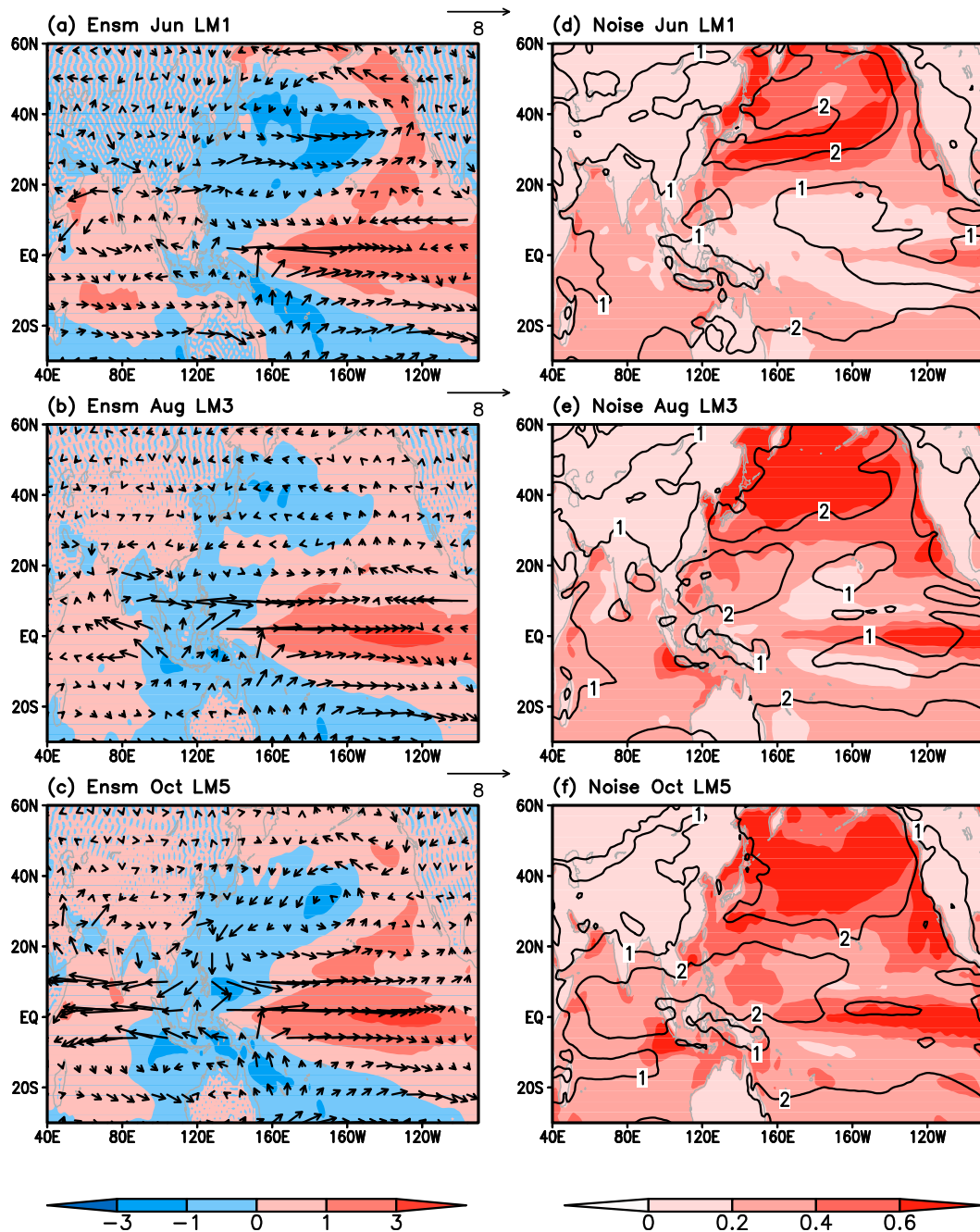## Composite for MSN1 MAY IC

FIG. 14. Composite differences with May ICs in different months in (a)–(c) ensemble mean SST (shading) and 850-hPa wind (vectors) between peaks and valleys of MSN PC1, and (d)–(f) composite of noise SST (shading) and 850-hPa zonal wind magnitude (contours) for peaks of MSN PC1.

positive SST anomalies propagate toward the equator through the wind–evaporation–SST (WES) feedback. By early spring, warm SST anomalies reach the equatorial Pacific and tend to grow through the ENSO-like feedback (Figs. 16h,j,l,n). This process is similar to the SFM for

ENSO triggering (Vimont et al. 2001, 2003). Again, the sign of anomalies does not matter for these correlation and regression patterns. In comparison to those for May ICs, the northern extratropical perturbations affect the tropical circulation more effectively than the southern
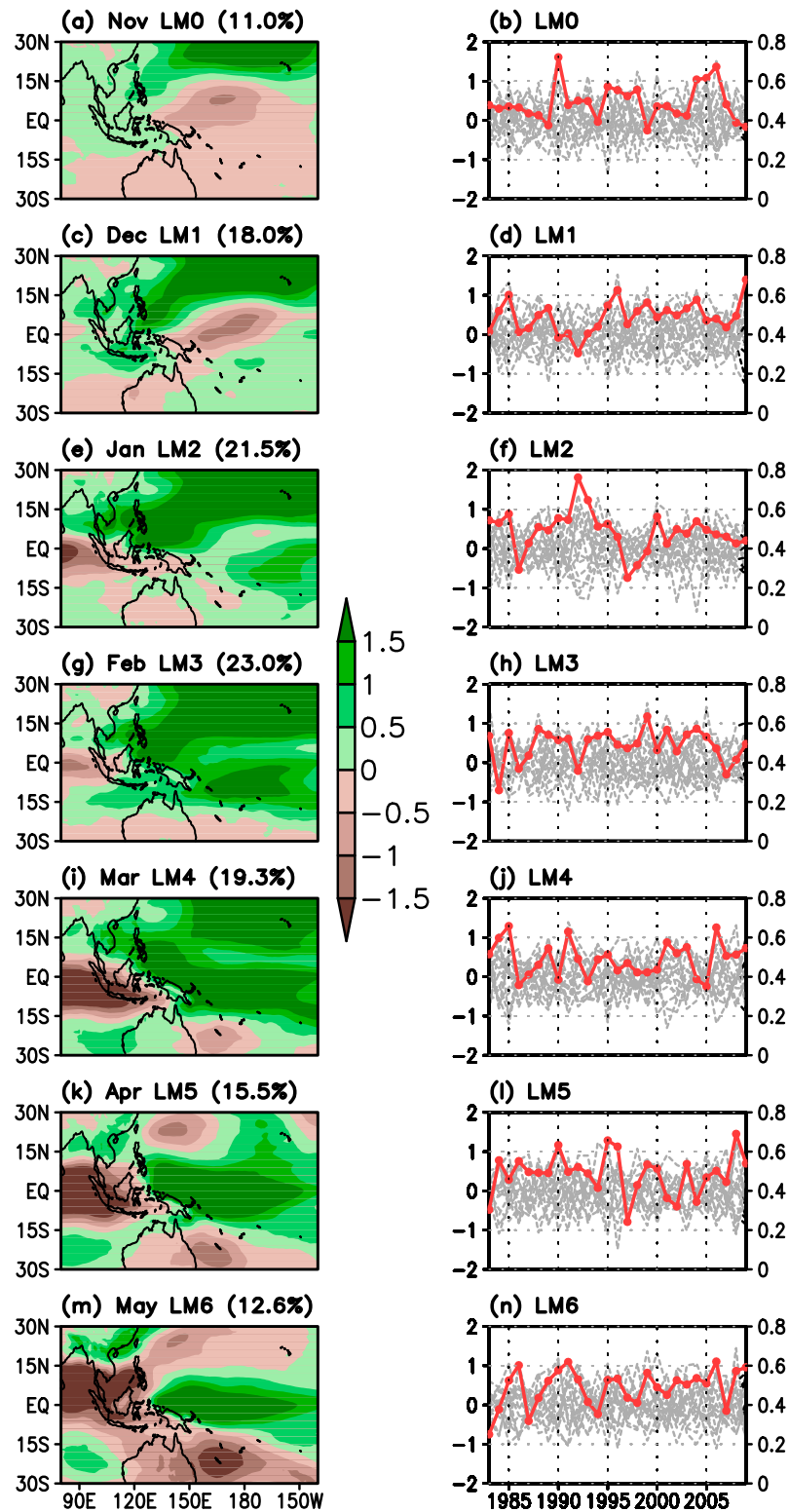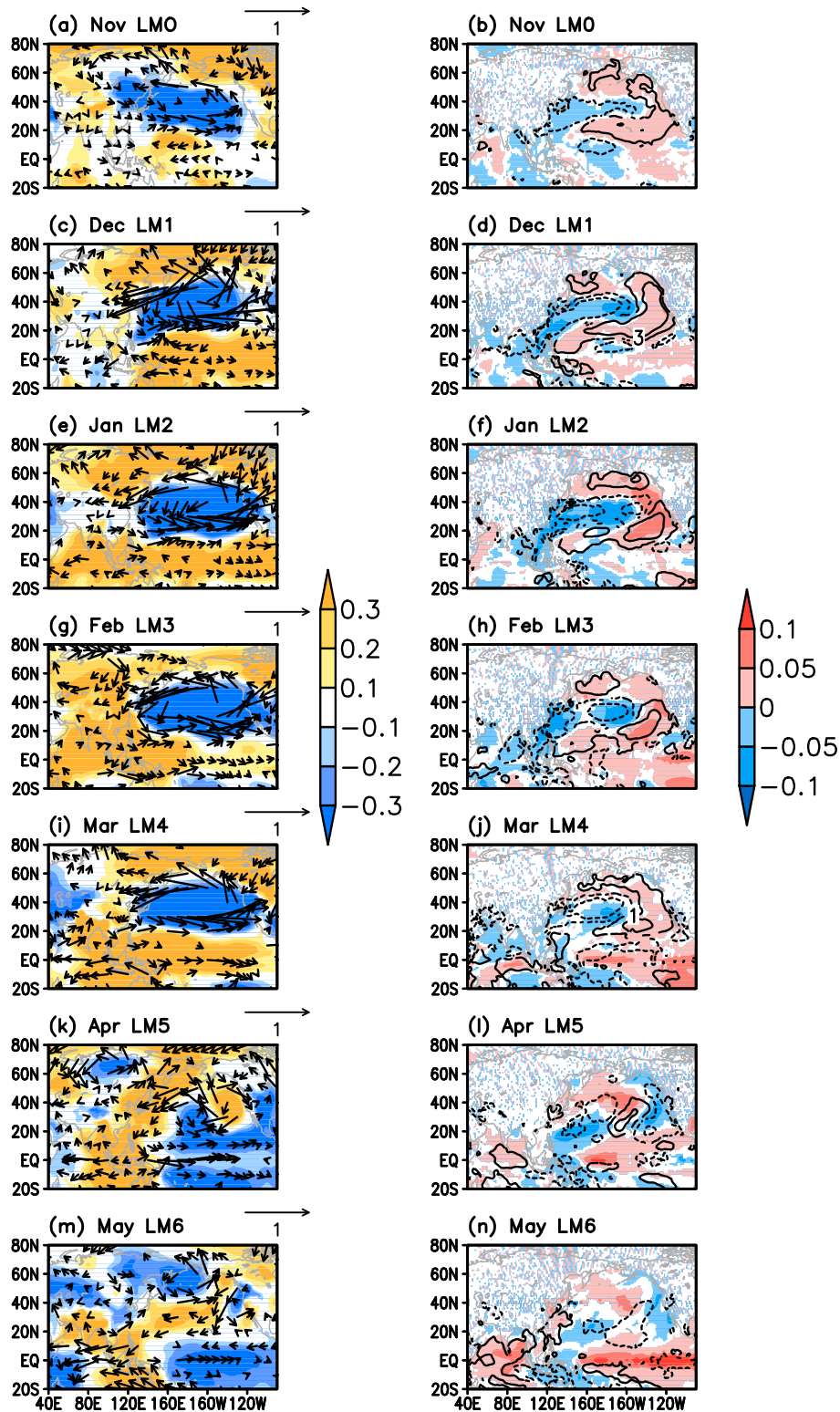
FIG. 15. As in Fig. 12, but for ICs in November.

FIG. 16. Correlations of noise SLP/SLHF with noise PC1s and regression of noise 850-hPa wind (m s^{-1})/SLHF (W m^{-2})/SST (K) against noise PC1s in of different lead months for T639 with ICs in November. (left) The patterns for SLP (shading) and 850-hPa wind (vectors), and (right) the patterns for SST (shading) and SLHF (contours). Only values exceeding the 95% confidence level are shown.
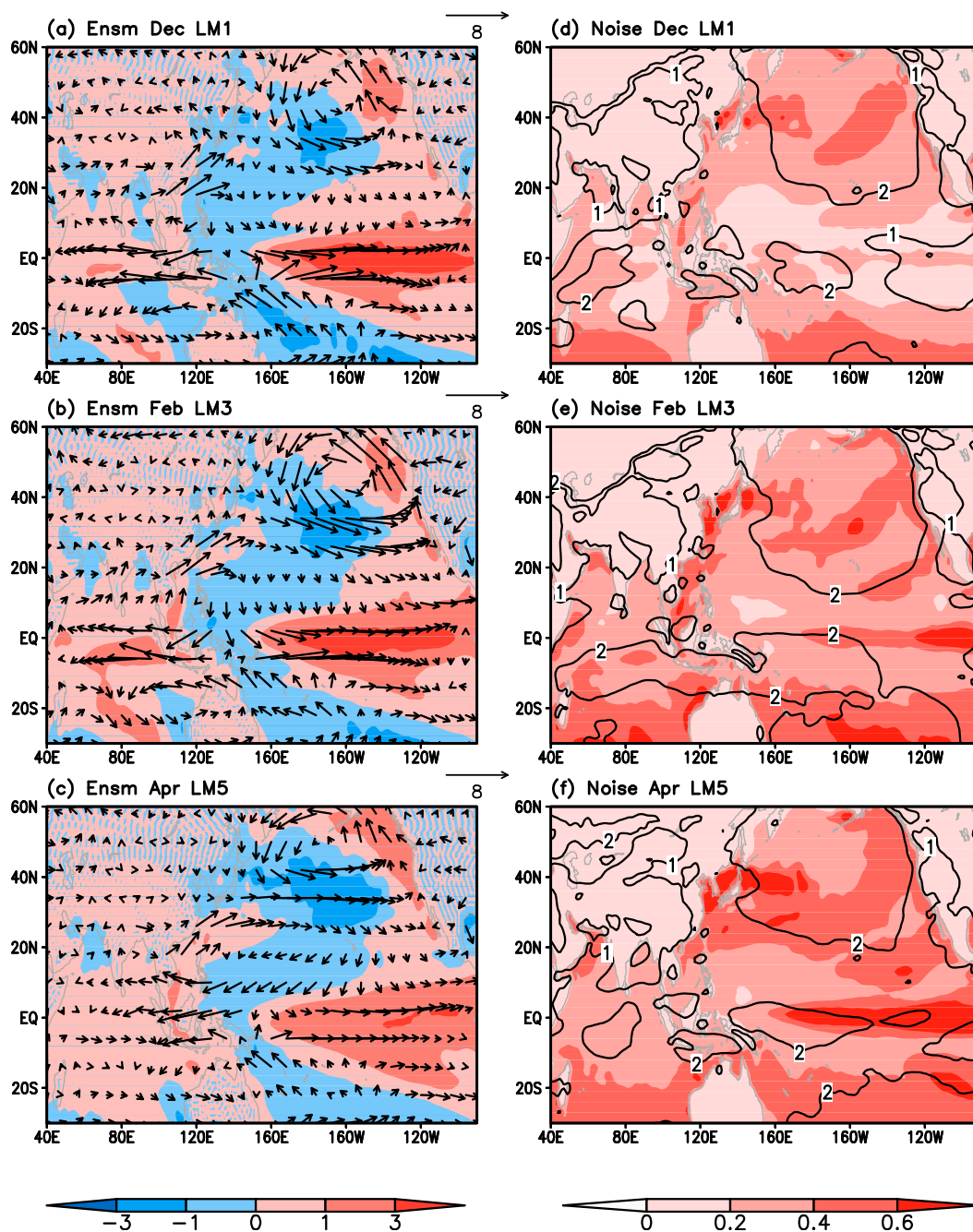
Composite for MSN1 NOV IC

FIG. 17. As in Fig. 14, but for November ICs.

ones and may play a major role in prediction uncertainty during the winter half of the year.

Similar features can also be seen from Fig. 17, which shows composite differences in ensemble mean SST and 850-hPa wind and the composite of noise SST and 850-hPa zonal wind magnitude for MSN PC1 with

November ICs. Composite figures for ensemble mean mainly show features of ENSO maturing phase, consistent with those for the most predictable patterns in November ICs (Figs. 17 and 8). Similar to the noise EOF patterns, the largest model spread is mainly located over the extratropical Northern Hemisphere and

then expands southward in the subsequent months (Fig. 17, right). The spread of wind noise over the equatorial Indo-Pacific region is enhanced in February (Fig. 17e). Consistently, the large SST spread reaches the equatorial Pacific in February and tends to grow during the spring season (Figs. 17e,f). Similar features appear in composite figures for the positive and negative ENSO events (figures not shown).

6. Discussion and conclusions

In this study, we investigate the seasonal evolution of the predictable patterns and the intraensemble variability of monthly 850-hPa zonal wind over the tropical Indo-Pacific region using Project Minerva hindcasts. The most predictable patterns are identified by applying MSN EOF analysis. We also obtain the dominant structures of the intraensemble variation at different leads of forecast and study their associated mechanisms.

The most predictable patterns from both May and November ICs are associated with ENSO and correspond to the development of ENSO. These most predictable patterns are well predicted by the model for all target months but with a relative minimum for the target months in summer resulting from the spring predictability barrier. The common feature for these most predictable patterns is the opposite sign loadings between the central-eastern equatorial Pacific and the equatorial IO. The loadings over the equatorial IO, however, weaken during the target months in summer and then strengthen during the fall months in May ICs. Correspondingly, the associated ocean–atmosphere anomalies show that the early predictable ENSO signals in late spring are associated with a weak or delayed onset of the Asian monsoon, and the relationship between ENSO and the monsoon is weakened as the prediction is extended into summer months. This weakened relationship may be responsible for the relatively lower prediction skill for the target months in summer. We find that the second most predictable patterns from November ICs are also closely linked to ENSO, but only for the ENSO decaying phase. The MSN PC2s are significantly correlated with the Niño-4 indices especially in the spring months, but are insignificantly correlated with the Niño-3 and Niño-3.4 indices because of the decaying SST anomalies over the eastern equatorial Pacific during the post-ENSO spring. These features depicted above are consistent with those in Zhang et al. (2018), indicating that the most predictable ENSO patterns are not sensitive to the forecast system resolution.

We find that the predictable signals in the second MSN modes from May ICs are mainly located over the WNP, which show a northward shift during the target months in summer and a southward shift in the target months in fall. Correspondingly, the associated ocean–atmosphere anomalies from May ICs show a northward shift of the WNP anomalous anticyclone/cyclone in the summer months, followed by a southward shift in the fall months, associated with the lifespan of the WNP monsoon. These predictable WNP patterns are also well predicted in Project Minerva hindcasts, but the prediction skill is much lower than those for the predictable ENSO patterns.

We also examine the intraensemble variability of 850-hPa zonal wind within the tropical Indo-Pacific region in Project Minerva hindcasts to identify the most likely disrupters of seasonal predictions. The intraensemble spread includes both initial state errors and noise-driven errors. Although it is difficult to distinguish errors generated by initial state or internal noise, since the latter is generated by the former in the model, we still can get some hints from this analysis. In fact, the noise distributions reflect the uncertainty of the initial states at short leads but are dominated by the model internal noise in longer leads. Therefore, the evolution in the patterns of the ensemble spread is influenced by the model dynamics. For the hindcasts with May ICs, the model spread is generated by the extratropical perturbations from the Southern Hemisphere in late spring. However, the location of large model spread appears to the north of the equator during the target months in summer, although the spread in the Southern Hemisphere persists. During the fall months, the intraensemble spread is characterized by the opposite wind anomalies over the equatorial Pacific and the IO, which are mainly associated with the SST anomalies in the central-eastern equatorial Pacific, the Walker circulation. The evolution of the intraensemble spread seems to be driven by the same dynamics that are responsible for the evolutions of predictable ENSO and WNP. Actually, the spatial structures of the first EOF modes of model noise data for the summer and fall months resemble the second and first predictable patterns, respectively, which reflects the noise-induced feedback difference among ensemble members. On the other hand, the noise patterns with November ICs are characterized by a coupled southward expansion of the extratropical atmospheric perturbations in the Northern Hemisphere from winter to early spring. The associated ocean–atmosphere anomalies from winter to early spring are similar to the process of SFM for ENSO triggering (Vimont et al. 2001, 2003). In comparison, the Northern Hemisphere extratropical perturbations affect the tropical circulation more effectively than the Southern Hemisphere ones, consistent with Ma et al. (2017b).

REFERENCES

Allen, M. R., and L. A. Smith, 1997: Optimal filtering in singular spectrum analysis. *Phys. Lett.*, **234A**, 419–428, https://doi.org/10.1016/S0375-9601(97)00559-8.

Balmaseda, M. A., M. K. Davey, and D. L. T. Anderson, 1995: Decadal and seasonal dependence of ENSO prediction skill. *J. Climate*, **8**, 2705–2715, https://doi.org/10.1175/1520-0442(1995)008<2705:DASDOE>2.0.CO;2.

——, K. Mogensen, and A. T. Weaver, 2013: Evaluation of the ECMWF ocean reanalysis system ORAS4. *Quart. J. Roy. Meteor. Soc.*, **139**, 1132–1161, https://doi.org/10.1002/qj.2063.

Barnston, A. G., and M. K. Tippett, 2013: Predictions of Nino3.4 SST in CFSv1 and CFSv2: A diagnostic comparison. *Climate Dyn.*, **41**, 1615–1633, https://doi.org/10.1007/s00382-013-1845-2.

——, ——, M. L. L'Heureux, S. Li, and D. G. DeWitt, 2012: Skill of real-time seasonal ENSO model predictions during 2002–11: Is our capability increasing? *Bull. Amer. Meteor. Soc.*, **93** (Suppl.), https://doi.org/10.1175/BAMS-D-11-00111.2.

Battisti, D. S., 1988: Dynamics and thermodynamics of a warming event in a coupled tropical atmosphere–ocean model. *J. Atmos. Sci.*, **45**, 2889–2919, https://doi.org/10.1175/1520-0469(1988)045<2889:DATOAW>2.0.CO;2.

Blumenthal, M. B., 1991: Predictability of a coupled ocean–atmosphere model. *J. Climate*, **4**, 766–784, https://doi.org/10.1175/1520-0442(1991)004<0766:POACOM>2.0.CO;2.

Cai, W., P. van Rensch, T. Cowan, and H. H. Hendon, 2011: Teleconnection pathways of ENSO and the IOD and the mechanisms for impacts on Australian rainfall. *J. Climate*, **24**, 3910–3923, https://doi.org/10.1175/2011JCLI4129.1.

Chang, C.-P., Y. Zhang, and T. Li, 2000: Interannual and interdecadal variations of the East Asian summer monsoon and tropical Pacific SSTs. Part I: Roles of the subtropical ridge. *J. Climate*, **13**, 4310–4325, https://doi.org/10.1175/1520-0442(2000)013<4310:IAIVOT>2.0.CO;2.

Chang, P., R. Saravanan, L. Ji, and G. C. Hegerl, 2000: The effect of local sea surface temperatures on atmospheric circulation over the tropical Atlantic sector. *J. Climate*, **13**, 2195–2216, https://doi.org/10.1175/1520-0442(2000)013<2195:TEOLSS>2.0.CO;2.

Chowdary, J. S., S.-P. Xie, J.-J. Luo, J. Hafner, S. Behera, Y. Masumoto, and T. Yamagata, 2011: Predictability of northwest Pacific climate during summer and the role of the tropical Indian Ocean. *Climate Dyn.*, **36**, 607–621, https://doi.org/10.1007/s00382-009-0686-5.

Dee, D. P., and Coauthors, 2011: The ERA-Interim reanalysis: Configuration and performance of the data assimilation system. *Quart. J. Roy. Meteor. Soc.*, **137**, 553–597, https://doi.org/10.1002/qj.828.

Hendon, H. H., M. C. Wheeler, and C. Zhang, 2007: Seasonal dependence of the MJO–ENSO relationship. *J. Climate*, **20**, 531–543, https://doi.org/10.1175/JCLI4003.1.

Hirst, A. C., 1986: Unstable and damped equatorial modes in simple coupled ocean–atmosphere models. *J. Atmos. Sci.*, **43**, 606–632, https://doi.org/10.1175/1520-0469(1986)043<0606:UADEMI>2.0.CO;2.

Hu, Z.-Z., and B. Huang, 2007: The predictive skill and the most predictable pattern in the tropical Atlantic: The effect of ENSO. *Mon. Wea. Rev.*, **135**, 1786–1806, https://doi.org/10.1175/MWR3393.1; Corrigendum, **135**, 3009, https://doi.org/10.1175/MWR3554.1.

Huang, B., 2004: Remotely forced variability in the tropical Atlantic Ocean. *Climate Dyn.*, **23**, 133–152, https://doi.org/10.1007/s00382-004-0443-8.

——, and J. L. Kinter III, 2002: Interannual variability in the tropical Indian Ocean. *J. Geophys. Res.*, **107**, 3199, https://doi.org/10.1029/2001JC001278.

——, and J. Shukla, 2007: Mechanisms for the interannual variability in the tropical Indian Ocean. Part II: Regional processes. *J. Climate*, **20**, 2937–2960, https://doi.org/10.1175/JCLI4169.1.

——, and ——, 2008: Interannual variability of the South Indian Ocean in observations and a coupled model. *Indian J. Mar. Sci.*, **37**, 13–34.

Jia, X., H. Lin, J.-Y. Lee, and B. Wang, 2012: Season-dependent forecast skill of the leading forced atmospheric circulation pattern over the North Pacific and North American region. *J. Climate*, **25**, 7248–7265, https://doi.org/10.1175/JCLI-D-11-00522.1.

——, ——, and X. Yao, 2014: The influence of tropical Pacific SST anomaly on surface air temperature in China. *J. Climate*, **27**, 1425–1444, https://doi.org/10.1175/JCLI-D-13-00176.1.

Jiang, X., S. Yang, J. Li, Y. Li, H. Hu, and Y. Lian, 2013: Variability of the Indian Ocean SST and its possible impact on summer western North Pacific anticyclone in the NCEP Climate Forecast System. *Climate Dyn.*, **41**, 2199–2212, https://doi.org/10.1007/s00382-013-1934-2.

Jin, F.-F., J. D. Neelin, and M. Ghil, 1994: El Niño on the devil's staircase: Annual subharmonic steps to chaos. *Science*, **264**, 70–72, https://doi.org/10.1126/science.264.5155.70.

Johnson, C., and N. Bowler, 2009: On the reliability and calibration of ensemble forecasts. *Mon. Wea. Rev.*, **137**, 1717–1720, https://doi.org/10.1175/2009MWR2715.1.

Karspeck, A. R., A. Kaplan, and M. A. Cane, 2006: Predictability loss in an intermediate ENSO model due to initial error and atmospheric noise. *J. Climate*, **19**, 3572–3588, https://doi.org/10.1175/JCLI3818.1.

Kinter, J. L., III, and Coauthors, 2013: Revolutionizing climate modeling with Project Athena: A multi-institutional, international collaboration. *Bull. Amer. Meteor. Soc.*, **94**, 231–245, https://doi.org/10.1175/BAMS-D-11-00043.1.

Kirtman, B. P., and Coauthors, 2014: The North American multimodel ensemble: Phase-1 seasonal-to-interannual prediction; phase-2 toward developing intraseasonal prediction. *Bull. Amer. Meteor. Soc.*, **95**, 585–601, https://doi.org/10.1175/BAMS-D-12-00050.1.

Kosaka, Y., S.-P. Xie, N.-C. Lau, and G. A. Vecchi, 2013: Origin of seasonal predictability for summer climate over the northwestern Pacific. *Proc. Natl. Acad. Sci. USA*, **110**, 7574–7579, https://doi.org/10.1073/pnas.1215582110.

Kug, J.-S., F.-F. Jin, K. P. Sooraj, and I.-S. Kang, 2008: State-dependent atmospheric noise associated with ENSO. *Geophys. Res. Lett.*, **35**, L05701, https://doi.org/10.1029/2007GL032017.

Larson, S. M., and B. P. Kirtman, 2015: Revisiting ENSO coupled instability theory and SST error growth in a fully coupled model. *J. Climate*, **28**, 4724–4742, https://doi.org/10.1175/JCLI-D-14-00731.1.

——, and ——, 2017: Drivers of coupled model ENSO error dynamics and the spring predictability barrier. *Climate Dyn.*, **48**, 3631–3644, https://doi.org/10.1007/s00382-016-3290-5.

Lau, K.-M., K.-M. Kim, and S. Yang, 2000: Dynamical and boundary forcing characteristics of regional components of the Asian summer monsoon. *J. Climate*, **13**, 2461–2482, https://doi.org/10.1175/1520-0442(2000)013<2461:DABFCO>2.0.CO;2.

Lau, N.-C., and M. J. Nath, 1996: The role of the "atmospheric bridge" in linking tropical Pacific ENSO events to extratropical SST anomalies. *J. Climate*, **9**, 2036–2057, https://doi.org/10.1175/1520-0442(1996)009<2036:TROTBI>2.0.CO;2.

Li, T., B. Wang, and L. Wang, 2016: Comments on "Combination mode dynamics of the anomalous northwest Pacific anticyclone." *J. Climate*, **29**, 4685–4693, https://doi.org/10.1175/JCLI-D-15-0385.1.

Liang, J., S. Yang, Z.-Z. Hu, B. Huang, A. Kumar, and Z. Zhang, 2009: Predictable patterns of the Asian and Indo-Pacific summer precipitation in the NCEP CFS. *Climate Dyn.*, **32**, 989–1001, https://doi.org/10.1007/s00382-008-0420-8.

Lin, H., G. Brunet, and J. Derome, 2008: Forecast skill of the Madden–Julian oscillation in two Canadian atmospheric models. *Mon. Wea. Rev.*, **136**, 4130–4149, https://doi.org/10.1175/2008MWR2459.1.

Lopez, H., and B. P. Kirtman, 2014: WWBs, ENSO predictability, the spring barrier and extreme events. *J. Geophys. Res. Atmos.*, **119**, 10 114–10 138, https://doi.org/10.1002/2014JD021908.

Luo, J.-J., S. Masson, S. K. Behera, and T. Yamagata, 2008: Extended ENSO predictions using a fully coupled ocean–atmosphere model. *J. Climate*, **21**, 84–93, https://doi.org/10.1175/2007JCLI1412.1.

——, R. Zhang, S. K. Behera, Y. Masumoto, F.-F. Jin, R. Lukas, and T. Yamagata, 2010: Interaction between El Niño and extreme Indian Ocean dipole. *J. Climate*, **23**, 726–742, https://doi.org/10.1175/2009JCLI3104.1.

Ma, J., S.-P. Xie, and H. Xu, 2017a: Intermember variability of the summer northwest Pacific subtropical anticyclone in the ensemble forecast. *J. Climate*, **30**, 3927–3941, https://doi.org/10.1175/JCLI-D-16-0638.1.

——, ——, and ——, 2017b: Contributions of the North Pacific meridional mode to ensemble spread of ENSO prediction. *J. Climate*, **30**, 9167–9181, https://doi.org/10.1175/JCLI-D-17-0182.1.

Madec, G., 2008: NEMO reference manual, ocean dynamics component: NEMO-OPA, version 3.0. ISPL Note du Pole de modélisation 27, 217 pp., http://www.nemo-ocean.eu/About-NEMO/Reference-manuals.

Manganello, J. V., and Coauthors, 2016: Seasonal forecasts of tropical cyclone activity in a high-atmospheric-resolution coupled prediction system. *J. Climate*, **29**, 1179–1200, https://doi.org/10.1175/JCLI-D-15-0531.1.

McPhaden, M. J., S. E. Zebiak, and M. H. Glantz, 2006: ENSO as an integrating concept in Earth science. *Science*, **314**, 1740–1745, https://doi.org/10.1126/science.1132588.

Molteni, F., and Coauthors, 2011: The new ECMWF seasonal forecast system (system 4). ECMWF Tech. Memo. 656, 49 pp.

Nitta, T., 1987: Convective activities in the tropical western Pacific and their impact on the Northern Hemisphere summer

circulation. *J. Meteor. Soc. Japan*, **65**, 373–390, https://doi.org/10.2151/jmsj1965.65.3_373.

Penland, C., 1996: A stochastic model of IndoPacific sea surface temperature anomalies. *Physica D*, **98**, 534–558, https://doi.org/10.1016/0167-2789(96)00124-8.

——, and P. D. Sardeshmukh, 1995: The optimal growth of tropical sea surface temperature anomalies. *J. Climate*, **8**, 1999–2024, https://doi.org/10.1175/1520-0442(1995)008<1999:TOGOTS>2.0.CO;2.

Philander, S. G. H., 1983: El Niño Southern Oscillation phenomena. *Nature*, **302**, 295–301, https://doi.org/10.1038/302295a0.

Ramage, C. S., 1968: Role of a tropical "Maritime Continent" in the atmospheric circulation. *Mon. Wea. Rev.*, **96**, 365–369, https://doi.org/10.1175/1520-0493(1968)096<0365:ROATMC>2.0.CO;2.

Rasmusson, E. M., and T. H. Carpenter, 1982: Variations in tropical sea surface temperature and surface winds associated with the Southern Oscillation/El Niño. *Mon. Wea. Rev.*, **110**, 354–384, https://doi.org/10.1175/1520-0493(1982)110<0354:VITSST>2.0.CO;2.

——, and ——, 1983: The relationship between the eastern equatorial Pacific sea surface temperatures and rainfall over India and Sri Lanka. *Mon. Wea. Rev.*, **111**, 517–528, https://doi.org/10.1175/1520-0493(1983)111<0517:TRBEEP>2.0.CO;2.

Reynolds, R. W., T. M. Smith, C. Liu, D. B. Chelton, K. S. Casey, and M. G. Schlax, 2007: Daily high-resolution blended analyses for sea surface temperature. *J. Climate*, **20**, 5473–5496, https://doi.org/10.1175/2007JCLI1824.1.

Rogers, J. C., 1981: The North Pacific Oscillation. *Int. J. Climatol.*, **1**, 39–57, https://doi.org/10.1002/joc.3370010106.

Rowell, D. P., C. K. Folland, K. Maskell, and M. N. Ward, 1995: Variability of summer rainfall over tropical North Africa (1906–92): Observations and modelling. *Quart. J. Roy. Meteor. Soc.*, **121**, 669–704, https://doi.org/10.1002/qj.49712152311.

Saha, S., and Coauthors, 2010: The NCEP Climate Forecast System Reanalysis. *Bull. Amer. Meteor. Soc.*, **91**, 1015–1057, https://doi.org/10.1175/2010BAMS3001.1.

Saji, N. H., B. N. Goswami, P. N. Vinayachandran, and T. Yamagata, 1999: A dipole mode in the tropical Indian Ocean. *Nature*, **401**, 360–363, https://doi.org/10.1038/43854.

Shi, L., H. H. Hendon, O. Alves, J.-J. Luo, M. Balmaseda, and D. Anderson, 2012: How predictable is the Indian Ocean dipole? *Mon. Wea. Rev.*, **140**, 3867–3884, https://doi.org/10.1175/MWR-D-12-00001.1.

Stuecker, M. F., A. Timmermann, F.-F. Jin, S. McGregor, and H.-L. Ren, 2013: A combination mode of the annual cycle and the El Niño/Southern Oscillation. *Nat. Geosci.*, **6**, 540–544, https://doi.org/10.1038/ngeo1826.

——, F.-F. Jin, A. Timmermann, and S. McGregor, 2015: Combination mode dynamics of the anomalous northwest Pacific anticyclone. *J. Climate*, **28**, 1093–1111, https://doi.org/10.1175/JCLI-D-14-00225.1.

——, A. Timmermann, F.-F. Jin, Y. Chikamoto, W. Zhang, A. T. Wittenberg, E. Widiasih, and S. Zhao, 2017: Revisiting ENSO/Indian Ocean dipole phase relationships. *Geophys. Res. Lett.*, **44**, 2481–2492, https://doi.org/10.1002/2016GL072308.

Sun, Y., and T. Zhou, 2014: How does El Niño affect the interannual variability of the boreal summer Hadley circulation? *J. Climate*, **27**, 2622–2642, https://doi.org/10.1175/JCLI-D-13-00277.1.

Sutton, R. T., S. P. Jewson, and D. P. Rowell, 2000: The elements of climate variability in the tropical Atlantic region. *J. Climate*, **13**, 3261–3284, https://doi.org/10.1175/1520-0442(2000)013<3261:TEOCVI>2.0.CO;2.

Tippett, M. K., A. G. Barnston, and S. Li, 2012: Performance of recent multimodel ENSO forecasts. *J. Appl. Meteor.*, **51**, 637–654, https://doi.org/10.1175/JAMC-D-11-093.1.

Torrence, C., and P. J. Webster, 1998: The annual cycle of persistence in the El Niño/Southern Oscillation. *Quart. J. Roy. Meteor. Soc.*, **124**, 1985–2004, https://doi.org/10.1002/qj.49712455010.

Trenberth, K. E., G. W. Branstator, D. Karoly, A. Kumar, N.-C. Lau, and C. Ropelewski, 1998: Progress during TOGA in understanding and modeling global teleconnections associated with tropical sea surface temperatures. *J. Geophys. Res.*, **103**, 14 291–14 324, https://doi.org/10.1029/97JC01444.

Tziperman, E., L. Stone, M. A. Cane, and H. Jarosh, 1994: El Niño chaos: Overlapping of resonances between the seasonal cycle and the Pacific ocean-atmosphere oscillator. *Science*, **264**, 72–74, https://doi.org/10.1126/science.264.5155.72.

van der Linden, P., and J. F. B. Mitchell, Eds., 2009: ENSEM-BLES: Climate change and its impacts: Summary of research and results from the ENSEMBLES project. ENSEMBLES Rep., Met Office Hadley Centre, 160 pp., http://ensembles-eu.metoffice.com/docs/Ensembles_final_report_Nov09.pdf.

Venzke, S., M. R. Allen, R. T. Sutton, and D. P. Rowell, 1999: The atmospheric response over the North Atlantic to decadal changes in sea surface temperature. *J. Climate*, **12**, 2562–2584, https://doi.org/10.1175/1520-0442(1999)012<2562:TAROTN>2.0.CO;2.

Vimont, D. J., D. S. Battisti, and A. C. Hirst, 2001: Footprinting: A seasonal connection between the tropics and mid-latitudes. *Geophys. Res. Lett.*, **28**, 3923–3926, https://doi.org/10.1029/2001GL013435.

——, J. M. Wallace, and D. S. Battisti, 2003: The seasonal footprinting mechanism in the Pacific: Implications for ENSO. *J. Climate*, **16**, 2668–2675, https://doi.org/10.1175/1520-0442(2003)016<2668:TSFMIT>2.0.CO;2.

Wang, B., and Q. Zhang, 2002: Pacific–East Asian teleconnection. Part II: How the Philippine Sea anomalous anticyclone is established during El Niño development. *J. Climate*, **15**, 3252–3265, https://doi.org/10.1175/1520-0442(2002)015<3252:PEATPI>2.0.CO;2.

——, R. Wu, and X. Fu, 2000: Pacific–East Asian teleconnection: How does ENSO affect East Asian climate? *J. Climate*, **13**, 1517–1536, https://doi.org/10.1175/1520-0442(2000)013<1517:PEATHD>2.0.CO;2.

——, ——, and T. Li, 2003: Atmosphere–warm ocean interaction and its impact on Asian–Australian monsoon variability. *J. Climate*, **16**, 1195–1211, https://doi.org/10.1175/1520-0442(2003)16<1195:AOIAII>2.0.CO;2.

Webster, P. J., and S. Yang, 1992: Monsoon and ENSO: Selectively interactive systems. *Quart. J. Roy. Meteor. Soc.*, **118**, 877–926, https://doi.org/10.1002/qj.49711850705.

——, A. M. Moore, J. P. Loschnigg, and R. R. Leben, 1999: Coupled ocean–atmosphere dynamics in the Indian Ocean during 1997–98. *Nature*, **401**, 356–360, https://doi.org/10.1038/43848.

Xie, P., and P. A. Arkin, 1997: Global precipitation: A 17-year monthly analysis based on gauge observations, satellite estimates, and numerical model outputs. *Bull. Amer. Meteor. Soc.*, **78**, 2539–2558, https://doi.org/10.1175/1520-0477(1997)078<2539:GPAYMA>2.0.CO;2.

Xie, S.-P., H. Annamalai, F. A. Schott, and J. P. McCreary Jr., 2002: Structure and mechanisms of South Indian Ocean climate variability. *J. Climate*, **15**, 864–878, https://doi.org/10.1175/1520-0442(2002)015<0864:SAMOSI>2.0.CO;2.

——, K. Hu, J. Hafner, H. Tokinaga, Y. Du, G. Huang, and T. Sampe, 2009: Indian Ocean capacitor effect on Indo–western Pacific climate during the summer following El Niño. *J. Climate*, **22**, 730–747, https://doi.org/10.1175/2008JCLI2544.1.

——, Y. Kosaka, Y. Du, K. M. Hu, J. S. Chowdary, and G. Huang, 2016: Indo-western Pacific ocean capacitor and coherent climate anomalies in post-ENSO summer: A review. *Adv. Atmos. Sci.*, **33**, 411–432, https://doi.org/10.1007/s00376-015-5192-6.

Zebiak, S. E., and M. A. Cane, 1987: A model El Niño–Southern Oscillation. *Mon. Wea. Rev.*, **115**, 2262–2278, https://doi.org/10.1175/1520-0493(1987)115<2262:AMENO>2.0.CO;2.

Zhang, C., and J. Gottshalck, 2002: SST anomalies of ENSO and the Madden–Julian oscillation in the equatorial Pacific. *J. Climate*, **15**, 2429–2445, https://doi.org/10.1175/1520-0442(2002)015<2429:SAOEAT>2.0.CO;2.

Zhang, T., S. Yang, X. Jiang, and P. Zhao, 2016a: Seasonal–interannual variation and prediction of wet and dry season rainfall over the Maritime Continent: Roles of ENSO and monsoon circulation. *J. Climate*, **29**, 3675–3695, https://doi.org/10.1175/JCLI-D-15-0222.1.

——, ——, ——, and B. Huang, 2016b: Roles of remote and local forcings in the variation and prediction of regional Maritime Continent rainfall in wet and dry seasons. *J. Climate*, **29**, 8871–8879, https://doi.org/10.1175/JCLI-D-16-0417.1.

——, B. Huang, S. Yang, and C. Laohalertchai, 2018: Seasonal dependence of the predictable low-level circulation patterns over the tropical Indo-Pacific domain. *Climate Dyn.*, **50**, 4263–4284, https://doi.org/10.1007/s00382-017-3874-8.

Zhu, J., B. Huang, M. A. Balmaseda, J. L. Kinter III, P. Peng, Z.-Z. Hu, and L. Marx, 2013: Improved reliability of ENSO hindcasts with multi-ocean analyses ensemble initialization. *Climate Dyn.*, **41**, 2785–2795, https://doi.org/10.1007/s00382-013-1965-8.

——, ——, A. Kumar, and J. L. Kinter III, 2015a: Seasonality in prediction skill and predictable pattern of tropical Indian Ocean SST. *J. Climate*, **28**, 7962–7984, https://doi.org/10.1175/JCLI-D-15-0067.1.

——, and Coauthors, 2015b: ENSO prediction in Project Minerva: Sensitivity to atmospheric horizontal resolution and ensemble size. *J. Climate*, **28**, 2080–2095, https://doi.org/10.1175/JCLI-D-14-00302.1.

Zuo, Z., S. Yang, Z.-Z. Hu, R. Zhang, W. Wang, B. Huang, and F. Wang, 2013: Predictable patterns and predictive skills of monsoon rainfall in Northern Hemisphere summer in NCEP CFSv2 reforecasts. *Climate Dyn.*, **40**, 3071–3088, https://doi.org/10.1007/s00382-013-1772-2.